

1 **Measurement report: Insights into the high temporal variability of**
2 **atmospheric carbon dioxide (CO₂) at a suburban station in the Indo-**
3 **Gangetic Plain**

4
5 Vimal Jose Vazhathara^{1, *}, Ravi Kumar Kunchala¹, Sajeev Philip¹, Jaswant Rathore¹, Dilip
6 Ganguly¹, Sagnik Dey^{1,2}, Tomoki Nakayama³, Yutaka Matsumi^{4,5} and Prabir K. Patra^{4,6}

7
8 ¹Centre for Atmospheric Sciences, Indian Institute of Technology Delhi, New Delhi, India.

9 ²Centre of Excellence for Research on Clean Air, Indian Institute of Technology Delhi, New
10 Delhi, India

11 ³Graduate School of Integrated Science and Technology, Nagasaki University, 1–14 Bunkyo-
12 machi, Nagasaki, Nagasaki, 852–8521, Japan

13 ⁴Research Institute for Humanity and Nature, Kyoto, Japan

14 ⁵Institute for Space-Earth Environmental Research, Nagoya University, Nagoya, Japan

15 ⁶Japan Agency for Marine-Earth Science and Technology (JAMSTEC), Yokohama, Japan.

16 *Correspondence to: Vimal Jose Vazhathara (vimaljosevazhathara@gmail.com), Centre for
17 Atmospheric Sciences, Indian Institute of Technology Delhi, New Delhi, 110016, India

18

19 **Abstract**

20 The unusual weather patterns and large anthropogenic emissions over the Indo-Gangetic Plain
21 (IGP) make it a significant hotspot of greenhouse gases like carbon dioxide (CO₂). Given the
22 significance of the IGP and highly populated Delhi National Capital Region (Delhi-NCR), a
23 GHG observatory was established at a suburban monitoring station in Sonipat, Haryana
24 (28.95°N, 77.10°E; 228m asl), about 45 km north of the Delhi state boundary. Using a laser-
25 based cavity ring-down spectroscopy (CRDS) technique, we measured CO₂ mole fraction from
26 February 2023 to January 2025. An annual average CO₂ mole fraction of 440.8±19.7 parts per
27 million (ppm) was recorded in 2024, which includes a strong seasonal variability, ranging from

28 422.6±23.3 ppm during the monsoon (June- September) to 456.4±30.8 ppm in post-monsoon
29 (October -November). A strong CO₂ diurnal amplitude of 29 ppm in May and 63 ppm in
30 October was observed mainly due to seasonal changes in boundary layer mixing (faster in May
31 than October) and biospheric activity (weaker in May than October). Further investigation of
32 the drivers of strong seasonal and diurnal CO₂ variability over IGP revealed a strong contrast
33 to other global monitoring stations in the same latitude band. A strong correlation between CO₂
34 and methane (CH₄) indicated a co-located emission source, while the strong positive correlation
35 between CO₂ and carbon monoxide (CO) during post-monsoon emerges due to emissions from
36 biomass burning. We demonstrated that the high temporal CO₂ variability in the IGP region is
37 driven by the complex interplay of local anthropogenic and biomass burning emissions,
38 biospheric fluxes, and prevailing meteorology.

39

40 **1. Introduction**

41 Carbon dioxide (CO₂) is the major greenhouse gas (GHG) contributing to climate change and
42 global warming (IPCC, 2021; Fawzy et al., 2020). Due to the long lifetime and high radiative
43 forcing potential, CO₂ can have a significant impact on global and regional climate (Wang et
44 al., 2010). The atmospheric CO₂ mole fraction has increased from 278 parts per million (ppm)
45 in the pre-industrial period to 427 ppm in 2025 (NOAA, <https://gml.noaa.gov>; Wigley (1983)).
46 This rapid increase in the atmospheric fraction of CO₂ is primarily due to the combustion of
47 fossil fuels, cement manufacture, deforestation, and other industrial processes (Stocker et al.,
48 2013; Huang et al., 2016; Yoro and Daramola, 2020). A comprehensive understanding of the
49 sources and sinks of CO₂ is critical for developing national policies to mitigate climate change
50 impacts.

51 India is the third-highest CO₂-emitting nation (8% of total global CO₂) in the last
52 decade, as reported by the Global Carbon Project (GCP) (Friedlingstein et al., 2025; Le Quéré
53 et al., 2018). In particular, the Indo-Gangetic Plain (IGP) region is one of the hotspots of
54 atmospheric CO₂ mole fraction, primarily due to large fossil fuel emissions and adverse
55 meteorology (Halder et al., 2021; Krishnapriya et al., 2025; Kuttippurath et al., 2022). Over the
56 past few decades, the IGP region has witnessed rapid urbanisation, industrialisation, and
57 agricultural intensification, leading to significant changes in land-use patterns and GHG
58 emissions (Yoro and Daramola, 2020). Mitigation of anthropogenic CO₂ emissions in the
59 highly populated IGP region is crucial to reducing the build-up of atmospheric CO₂ mole

60 fractions. Gaining a better understanding of the magnitude of CO₂ sources and sinks and the
61 local drivers of CO₂ temporal variability over the IGP region is therefore important.

62

63 Continuous monitoring of ground-based CO₂ is of utmost importance for inverse
64 modelling approaches to understand local-to-regional-scale sources and sinks of CO₂.
65 Although GHG mole fractions have been monitored worldwide for decades, GHG monitoring
66 stations in India are limited (Kunchala et al., 2025; Chakraborty et al., 2020; Kumar et al.,
67 2021; Patra et al., 2013; Tiwari et al., 2013). The Cape Rama (15.08° N, 73.83° E) station,
68 situated on India's southwest coast, was the first Indian monitoring station to track CO₂ mole
69 fraction from 1993 to 2002 (Bhattacharya et al., 2009; Patra et al., 2011; Rayner et al., 2008).
70 Recently, several monitoring stations have been established over different parts of India to
71 measure the GHGs (Chandra et al., 2016; Jain et al., 2021; Mahesh et al., 2015; Metya et al.,
72 2021; Nomura et al., 2021; Pathakoti et al., 2023; Sreenivas et al., 2016; Thilakan et al., 2023;
73 Tiwari et al., 2014). Studies have also been conducted using aircraft-based measurements
74 (Niwa et al., 2012; Patra et al., 2011; Schuck et al., 2012; Zhang et al., 2007) and satellite data
75 products (Das et al., 2023; Kunchala et al., 2022; Nalini et al., 2019; Philip et al., 2022; Xiong
76 et al., 2009). The incorporation of regional in situ and aircraft-based measurements, along with
77 satellite columnar CO₂ retrievals, reduced uncertainties in top-down CO₂ flux estimates (Huang
78 et al., 2008; Niwa et al., 2012; Zhang et al., 2014).

79 To comprehensively understand temporal CO₂ variability and its drivers in the western
80 IGP region, we have conducted atmospheric CO₂ mole fraction measurements at Sonipat, a
81 suburban station in the IGP region upwind of Delhi. The continuous measurements from
82 February 2023 to January 2025 were conducted using laser-based cavity ring-down
83 spectroscopy. Here, we investigate the novel characteristics of the seasonal and diurnal
84 variability of atmospheric CO₂ mole fraction at Sonipat. We then identify the key drivers of
85 the observed temporal CO₂ variability in the region.

86

87 **2. Materials and methods**

88 **2.1 Monitoring station**

89 The measurements in this study were carried out at the Indian Institute of Technology Delhi
90 (IIT Delhi) Centre for Atmospheric Sciences (CAS) - Atmospheric Observatory situated at
91 Sonipat campus (28.95°N, 77.10°E, 228m asl). Sonipat is an upwind suburban region of the
92 Delhi-NCR, situated in the northern Indian state of Haryana, approximately 45 kilometres north
93 of Delhi. The monitoring station is surrounded by agricultural fields, a National Highway, and

94 academic institutions (Rathore et al., 2025). Figure 1 shows the location map of the monitoring
95 station. The climatic conditions over this site are similar to Delhi which has sweltering
96 summers (March-May), damp or moist monsoons (June - September), and extreme winters.
97 Similar to Delhi, this region also has frequent haze and smog with low visibility during winter
98 (December - February) and post-monsoon (October - November) seasons. During the post-
99 monsoon season, Sonipat experiences large transport of pollutants from the North-West
100 direction. In addition to the pollutant transport, several local emission sources exist in the
101 region, such as small industries, vehicular sources, and local biomass burning affecting short-
102 lived air pollutants (Rathore et al., 2025).

103

104 **2.2 Local measurements**

105 **2.2.1 GHG measurements**

106 This study utilised the PICARRO G2301 GHG analyser to measure major atmospheric GHG
107 mole fractions. The PICARRO analyser employs the Cavity Ring-Down Spectroscopy (CRDS)
108 technique at 0.5 Hz to measure CO₂ mole fraction. The CRDS technique utilises the ring-down
109 time of light intensity within the cavity to determine the mole fraction of CO₂, a method
110 fundamentally different from other measurement techniques such as Non-dispersive Infrared
111 Spectroscopy (NDIR) and Fourier Transform Infrared Spectroscopy (FTIR). The long sample
112 interaction path length (approximately 20 km) is a characteristic of CRDS, which enhances
113 sensitivity compared to conventional techniques based on light-intensity absorption. The cavity
114 pressure operates at a very low pressure of 140 Torr. This isolates a single spectral feature with
115 a resolution of 0.0003 cm⁻¹, ensuring a linear relationship between peak height or area and mole
116 fraction. The CRDS provides precise, highly sensitive measurements of gases in ambient air
117 with a temporal resolution of 5 seconds. The technique has been well validated for measuring
118 atmospheric CO, CO₂, and CH₄ mole fractions globally and at some Indian monitoring stations
119 (Chandra et al., 2016; Chen et al., 2013; Jain et al., 2021).

120 The standard cavity temperature of 45°C (throughout the measurement period) ensures
121 the necessary etalon mechanical stability of the measurement cavity. The sample air was taken
122 from the top of the building and above the tree canopy (5 meters above the instrument housing)
123 through a Teflon (PTFE) tube with an inner diameter of 3 mm using an external vacuum pump
124 with ~400 SCCM flow rate (residence time ~5.9 s). The air intake height is about 248 m.

125 The Sonipat station, lying on the upwind side of Delhi, is a suburban station with
126 relatively cleaner air compared to the urban city centre. However, Sonipat cannot be considered
127 a pristine site due to the impact of local emissions from nearby industries and national

128 highways. We adopted (1) the fifth percentile of the daily data to characterise background mole
129 fraction at the site (Ammoura et al., 2014; Chandra et al., 2016; Jain et al., 2021), and (2) the
130 adaptive diurnal minimum variation selection (ADVS) method that considers the diurnal
131 minimum value as the daily background value (Apadula et al., 2019; Yuan et al., 2018). In this
132 study, the comparison between the fifth percentile and the ADVS methods showed similar CO₂
133 background values (see Fig. S1), and the ADVS method was used for further analysis. The
134 excess CO₂ mole fractions were then estimated by subtracting the hourly averaged values of
135 CO₂ from the background mole fraction.

136 The measurements of the atmospheric CH₄ mole fraction were also conducted with the
137 PICARRO G2301 GHG analyser. The GHG analyser employs the CRDS at 0.5 Hz to measure
138 CH₄ mole fraction. The mole fractions of CH₄ were determined using the ring-down time of
139 light intensity, similar to CO₂ mole fractions. Calibration was performed following the
140 guidelines of the National Oceanic and Atmospheric Administration Earth System Research
141 Laboratories (NOAA-ESRL, 2020) and the Integrated Carbon Observation System (ICOS)
142 protocol (Laurent, 2020), using NOAA standard calibration cylinders. Further details of the
143 calibration process are provided in Supplementary Section S1.

144

145 **2.2.2 Trace gas measurements**

146 In addition to the measurements of CO₂ and CH₄, we also utilised the measurements of trace
147 gases to establish the species interrelationships and to identify drivers of GHG sources. We
148 used a compact air-quality measurement instrument with gas sensors (CUPI-G) to continuously
149 measure air pollutants, including fine particulate matter (PM_{2.5}), nitric oxide (NO), nitrogen
150 dioxide (NO₂), and carbon monoxide (CO). The sensors used in CUPI-G are a palm-sized
151 optical PM_{2.5} sensor developed by Panasonic, a CO-B4 Carbon Monoxide Sensor, and an NO-
152 B4 Nitric Oxide Sensor developed by Alphasense. The sensitivity of the PM_{2.5} and CO sensors
153 was evaluated in Nagasaki, Japan, through intercomparisons with reference-grade instruments
154 employing a beta attenuation monitor (BAM) for PM_{2.5} and non-dispersive infrared (NDIR)
155 spectroscopy for CO measurements (Figure S1). The estimated unit-to-unit variability was 29%
156 for PM_{2.5} sensors and 21% for CO sensors. Further details on the sensor specifications and the
157 calibration methodology are described in Mangaraj et al. (2025).

158

159 **2.2.3 Local meteorology measurements**

160 A Vaisala Ceilometer lidar CL61 provides real-time measurements of cloud base height (CBH)
161 for up to five layers, along with depolarisation measurements, under all weather conditions. To

162 determine the Planetary boundary layer height (PBLH) from the range-corrected attenuated
163 backscatter data, the gradient method (Summa et al., 2013) and the Wavelet Covariance
164 Transform (WCT) method (Baars et al., 2008) were employed. Further details on PBLH
165 calculations can be found in Rathore et al., (2025). An automatic weather station (AWS) by
166 Geonica, installed on the I-Tech building rooftop, collected meteorological data at 5-minute
167 intervals. The data, including ambient temperature, relative humidity (RH), atmospheric
168 pressure, wind speed and direction, precipitation, and incoming solar radiation, were retrieved
169 using Datagraph-W4K 2.1.3.0 software and exported in CSV format. All sensors were
170 meticulously calibrated and regularly cleaned to ensure accuracy and reliability.

171

172 **2.3 Auxiliary data**

173 **2.3.1 ObsPack Data**

174 To compare the seasonality of atmospheric CO₂ of Sonipat with other non-Indian sites in the
175 same latitudinal band, we used selected sites from the
176 obspack_co2_1_GLOBALVIEWplus_v10.1_2024-11-13 (Schuldt et al., 2024). The data was
177 averaged for five years from 2018 to 2022 for all stations except Boulder Atmospheric
178 Observatory, Colorado, (2011-2016), to compare the seasonality over different locations across
179 the globe.

180

181 **2.3.2 Satellite CO₂ retrievals**

182 Along with the ground-based in situ CO₂ measurements at the Sonipat monitoring station, we
183 also used column average dry air CO₂ mole fraction (XCO₂) retrievals from the Orbiting
184 Carbon Observatory-2 and 3 satellites (OCO-2 and OCO-3) (Crisp et al., 2017; Eldering et al.,
185 2017). We used the bias-corrected OCO-2 v11.1r data product for the period from February
186 2023 to December 2024. The OCO-3 satellite provides XCO₂ data at a repeat cycle of 16 days
187 with a spatial resolution of 1.60 km × 2.25 km (nadir observation), which increases the swath
188 area from ~3.0 km² to ~3.5 km². We used the bias-corrected OCO-3 v10.4r data product
189 (Eldering et al., 2019; Srivastava et al., 2020) for the period from February 2023 to December
190 2024.

191

192 **2.3.3 FluxSat GPP**

193 To study the Gross Primary Production (GPP) fluxes over Sonipat, we used FluxSat v2.2 native
194 GPP product computed at the spatio-temporal resolution of the MCD43C data set (daily at
195 0.05° spatial resolution (Schaaf et al., 2002; Wang et al., 2018). FluxSat v2.2 has been derived

196 from the MODerate resolution Imaging Spectroradiometer (MODIS) instruments on the NASA
197 Terra and Aqua satellites using the collection 6.1 MCD43C Bidirectional Reflectance
198 Distribution Function (BRDF)-Adjusted Reflectances (NBAR) (Joiner et al., 2018; Joiner and
199 Yoshida, 2020; Schaaf and Wang, 2021). FluxSat v2.2 is “calibrated” using a set of the
200 FLUXNET 2015 and OneFlux tier 1 (publicly released) eddy covariance (EC) data and has
201 been compared with independent data (i.e., not used in the calibration) as validation. We used
202 Global Gross Primary Production (GPP) estimates for 2023 in this study.

203

204 **2.3.4 Ecosystem-proxy variables**

205 We used two key ecosystem proxy variables to examine the carbon cycle dynamics at the
206 Sonipat station and in the IGP region. The Normalised Difference Vegetation Index (NDVI)
207 version 5 data from the Advanced Very High Resolution Radiometer (AVHRR) was used here
208 (Vermote and NOAA CDR Program, 2018). The NDVI CDR summarises surface vegetation
209 coverage activity based on measurements in the red and near-infrared spectral bands at daily
210 intervals and at a spatial resolution of $0.05^\circ \times 0.05^\circ$.

211 To understand the photosynthetic capacity of the regional ecosystem to assimilate
212 atmospheric CO₂, we used Solar-Induced Chlorophyll Fluorescence (SIF) retrievals from the
213 OCO-2 satellite (Frankenberg et al., 2014). The OCO-2 provides SIF data at a temporal
214 resolution of 16 days and a spatial resolution of 1.35 km × 2.25 km. The estimation of SIF
215 relies on evaluating the in-filling of solar Fraunhofer lines at 757 nm and 770.1 nm surrounding
216 the O₂ A-band (Frankenberg et al., 2014; Sun et al., 2018). We used bias-corrected SIF data
217 from OCO-2 v11r and v11.2r SIF data products.

218

219 **2.4 Models**

220 **2.4.1 JAMSTEC's MIROC version 4 atmospheric chemistry-transport model (MIROC4- 221 ACTM)**

222 We used the Model for Interdisciplinary Research on Climate version 4 (MIROC4),
223 atmospheric general circulation model (AGCM)-based chemistry-transport model (MIROC4-
224 ACTM; Patra et al., 2018), to simulate CO₂ mole fraction for this study. Simulations were
225 performed at a horizontal resolution of T42 spectral truncations ($\sim 2.8^\circ$ latitude–longitude grid)
226 with 67 vertical hybrid-pressure layers between the Earth's surface and 0.0128 hPa (~ 80 km).
227 CO₂ tracers were simulated corresponding to fossil fuel combustion (FFCO₂), land biosphere
228 fluxes (LBCO₂), fire emissions (CO_{2fire}), and ocean exchanges (CO_{2ocean}) from different prior
229 (bottom-up) emissions sets (Chandra et al., 2022). FFCO₂ was simulated using the gridded

230 fossil fuel emission dataset (GridFED; Jones et al., 2021). LBCO₂ tracers were simulated using
231 two sets of terrestrial biosphere fluxes from the Carnegie-Ames-Stanford Approach (CASA)
232 biogeochemical model (Randerson et al., 1997) and Vegetation Integrative Simulator for Trace
233 Gases (VISIT) (Ito, 2019).

234

235 **2.4.2 CarbonTracker (CT) inverse model**

236 To understand the temporal pattern of atmospheric CO₂ mole fraction over the study station
237 and the IGP region, we used simulated CO₂ mole fraction from an inverse modelling
238 framework CarbonTracker (CT) (Peters et al., 2005). Here, we used the CarbonTracker 2022
239 release (CT2022), which incorporated two-way nesting of the offline atmospheric tracer
240 transport model TM5, supporting coarse-resolution global data and high-resolution regional
241 data (Krol et al., 2004). The TM5 model in CT2022 was driven with meteorology from the
242 ERA-interim reanalysis provided by the European Center for Medium-Range Weather
243 Forecasts (ECMWF). The CT2022 inverse model simulated atmospheric CO₂ mole fraction by
244 correcting the prior specifications of CO₂ sources and sinks in the model by assimilating global
245 in situ observations. In this study, we used the CT2022-simulated CO₂ mole fraction from
246 February 2023 to October 2023.

247

248 **2.4.3 GEOS-Chem inverse model**

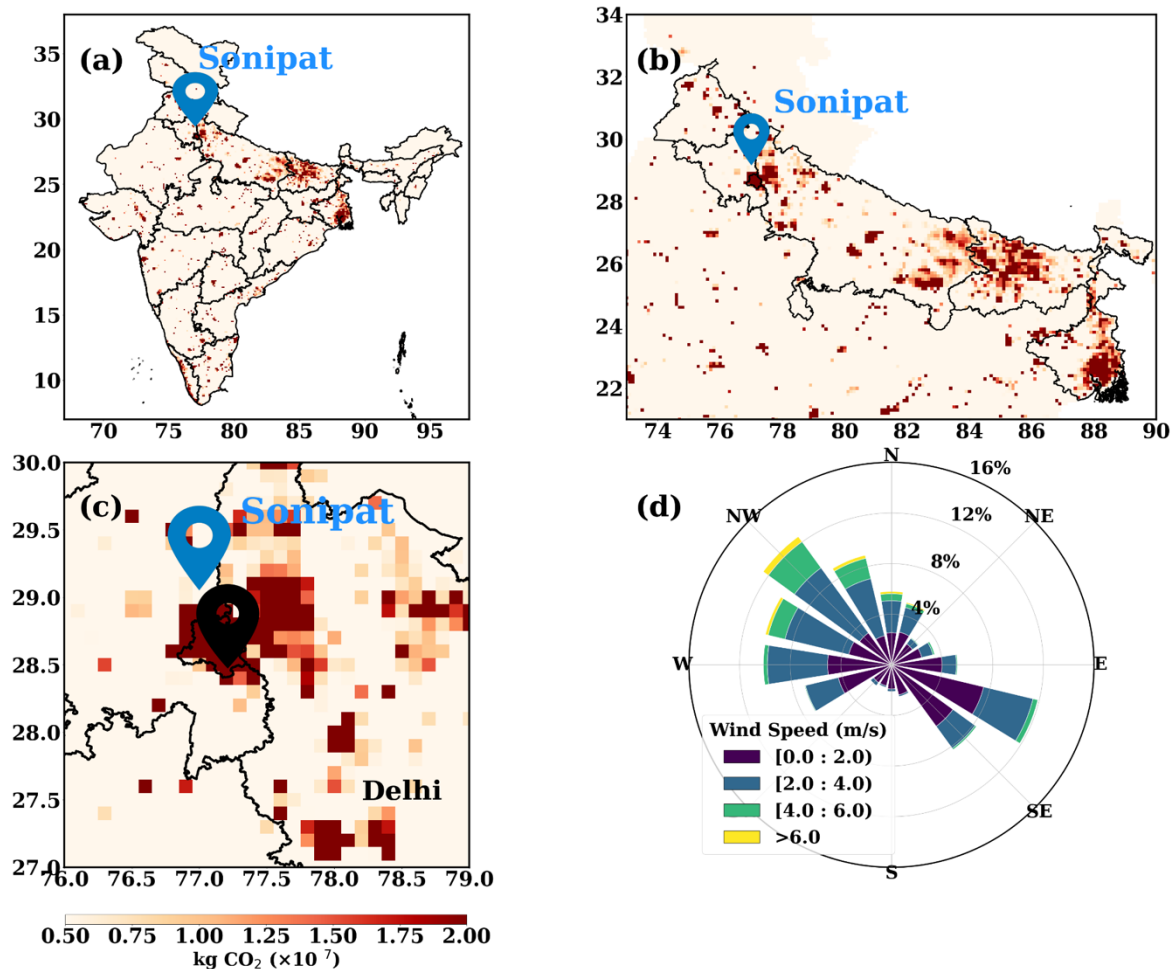
249 To study the seasonality of the fluxes over Sonipat, we used a four-dimensional variational
250 (4D-Var) assimilation system with the GEOS-Chem global chemical transport model
251 (CTM; Philip et al., 2019, 2022). The GEOS-Chem 4D-Var system was constrained with XCO₂
252 retrievals from the OCO-2 satellite (Philip et al., 2022), following the protocol of the OCO-2
253 v10 Multi-model Intercomparison Project (MIP) (Byrne et al., 2017; Liu et al., 2014). The Net
254 Ecosystem Exchange (NEE) fluxes for 2023 at a spatial resolution of 1° × 1°, constrained with
255 the OCO-2 Land Nadir and Land Glint observational modes are used here.

256

257 **2.4.4 Mi CASA terrestrial biospheric model**

258 We also used simulated CO₂ fluxes from a terrestrial biospheric model (TBM) in this study.
259 The Más informada Carnegie-Ames-Stanford-Approach (Mi CASA) model (Weir, 2024), a
260 comprehensive update to the CASA – Global Fire Emissions Database, version 3 (CASA-
261 GFED3) product, was utilised here (Chen et al., 2023; Potter et al., 1993). Mi CASA provides
262 daily global data at 0.1° resolution from January 2001 to December 2023. This includes carbon
263 flux variables from sources such as net primary production (NPP), heterotrophic respiration

264 (Rh), wildfire emissions (FIRE), and fuel wood burning emissions (FUEL). The model is
 265 driven with meteorological data from NASA's Modern-Era Retrospective analysis for Research
 266 and Application, Version 2 (MERRA-2).



267
 268 **Figure 1:** Anthropogenic CO₂ emissions over (a) India (b) IGP and (c) Sonipat/Delhi derived
 269 from the EDGAR emission inventory for 2021. (d) Annually averaged wind patterns over
 270 Sonipat for February 2023 – January 2024.

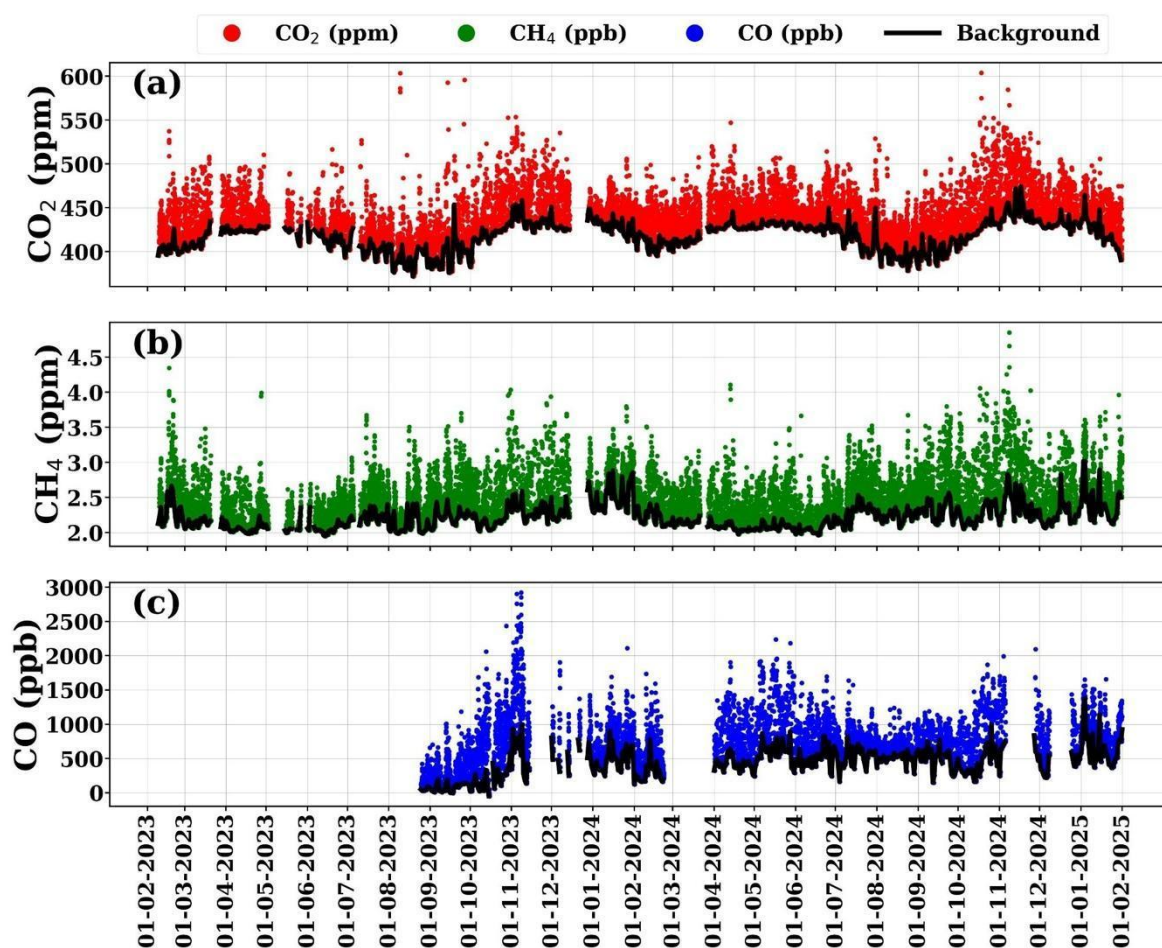
271
 272

273 3. Results and discussions

274 3.1 CO₂ measurements at Sonipat station

275 Figures 1(a-c) illustrate the annual mean anthropogenic CO₂ emissions over India, IGP and
 276 Delhi/Sonipat for 2021 based on the EDGAR emission inventory, a major hotspot of
 277 anthropogenic CO₂ emissions. The dominant wind direction over Sonipat was from the

278 northwest during the study period, highlighting influence from upwind sources of pollution and
 279 greenhouse gases (Figure 1d). Seasonal changes in meteorological parameters (air temperature,
 280 relative humidity, rainfall and wind; Figures S2 and S3) were also analysed alongside CO₂ to
 281 better understand the role of meteorology in Sonipat. In this study, we focus on seasonal and
 282 diurnal CO₂ variability and compare these patterns with those at other stations in India and in
 283 the same latitudinal band across the globe to uncover the unique aspects of CO₂ dynamics over
 284 Sonipat and the IGP.



285
 286 **Figure 2:** (a) Hourly averaged time series of atmospheric (a) CO₂, (b) CH₄, and (c) CO mole
 287 fraction for the study period (February 2023 to January 2025) over Sonipat. The thick black
 288 line represents the background mole fraction estimated using the ADVS method. CO₂ and CH₄
 289 measurements were made using a Picarro GHG analyser, and CO measurements were made
 290 using CUPI-G sensor

291
 292 Figure 2 presents the hourly averaged time series of atmospheric (a) CO₂, (b) CH₄, and
 293 (c) CO mole fractions at Sonipat during the study period (February 2023 to January 2025).

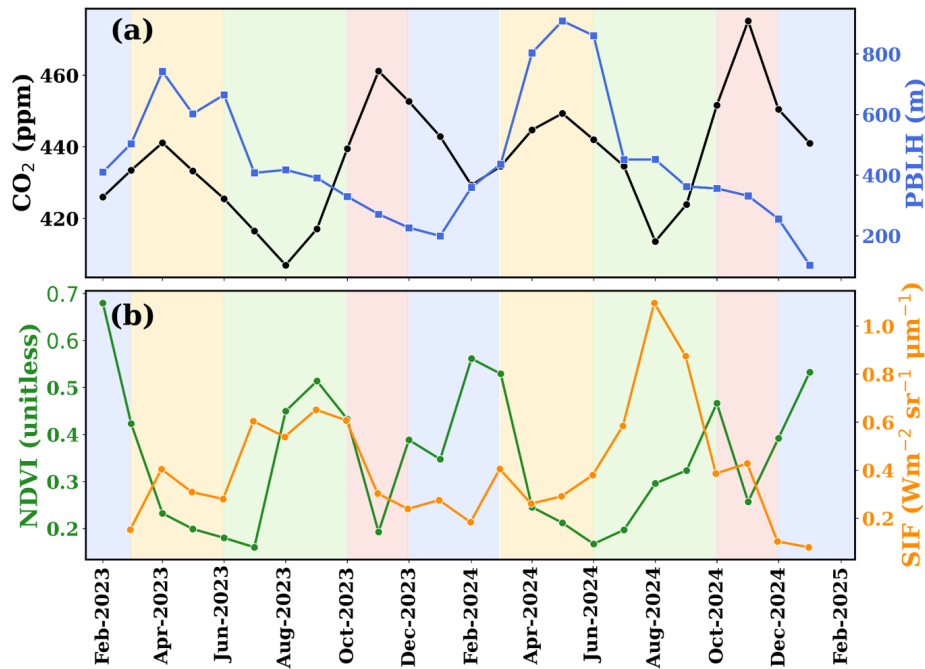
294 Hourly CO₂ mole fractions range from ~380 ppm to ~550 ppm, indicating strong monthly
295 variations in CO₂ mole fractions at the monitoring station. The lowest CO₂ mole fractions were
296 observed from July to August, which coincided with weak CO and strong CH₄ values. The
297 highest mole fractions of CO₂ were observed from October to November, coinciding with the
298 highest mole fractions of CO and CH₄. We found an annual mean CO₂ mole fraction of
299 440.8±19.7 ppm for 2024 and compared it with those from other monitoring stations across
300 India (Table S1). Interestingly, despite differences in site characteristics, the annual mean CO₂
301 levels at rural stations like Gadanki and urban stations like Ahmedabad are comparable,
302 whereas Sonipat shows distinctly higher values.

303 **3.2 Seasonal variability**

304 **3.2.1 Seasonality of in situ observations**

305 Figure 3 shows the monthly mean atmospheric CO₂ mole fractions during the study period. A
306 shaded background has been used to distinguish the seasonal regimes used in this study. The
307 monthly mean CO₂ mole fraction shows a maximum in November (post-monsoon season) and
308 a minimum in August (monsoon season) in both years. The observed seasonal mean of CO₂
309 during different seasons were 440.8±19.7 ppm (pre-monsoon), 422.6±23.3 ppm (monsoon),
310 456.4±30.8 ppm (post-monsoon), and 440.5±19.7 ppm (winter).

311 The seasonal change in CO₂ mole fractions over the monitoring station is governed by
312 the strength of emission sources, photosynthetic activity (biospheric fluxes), local meteorology
313 and atmospheric transport. The planetary boundary layer height (PBLH), which is determined
314 by local meteorology, strongly influences CO₂ mole fractions. PBL is the lowest layer within
315 the troposphere, where temperature and wind speed variations are integral in modulating its
316 height. During pre-monsoon, deep convection due to the well-developed PBLH from the
317 surface to the upper troposphere results in lower mole fractions of CO₂, while the weakly
318 developed PBLH in winter leads to higher CO₂ (Baker et al., 2012; Kar et al., 2004; Park et al.,
319 2009; Patra et al., 2011; Randel and Park, 2006).



320

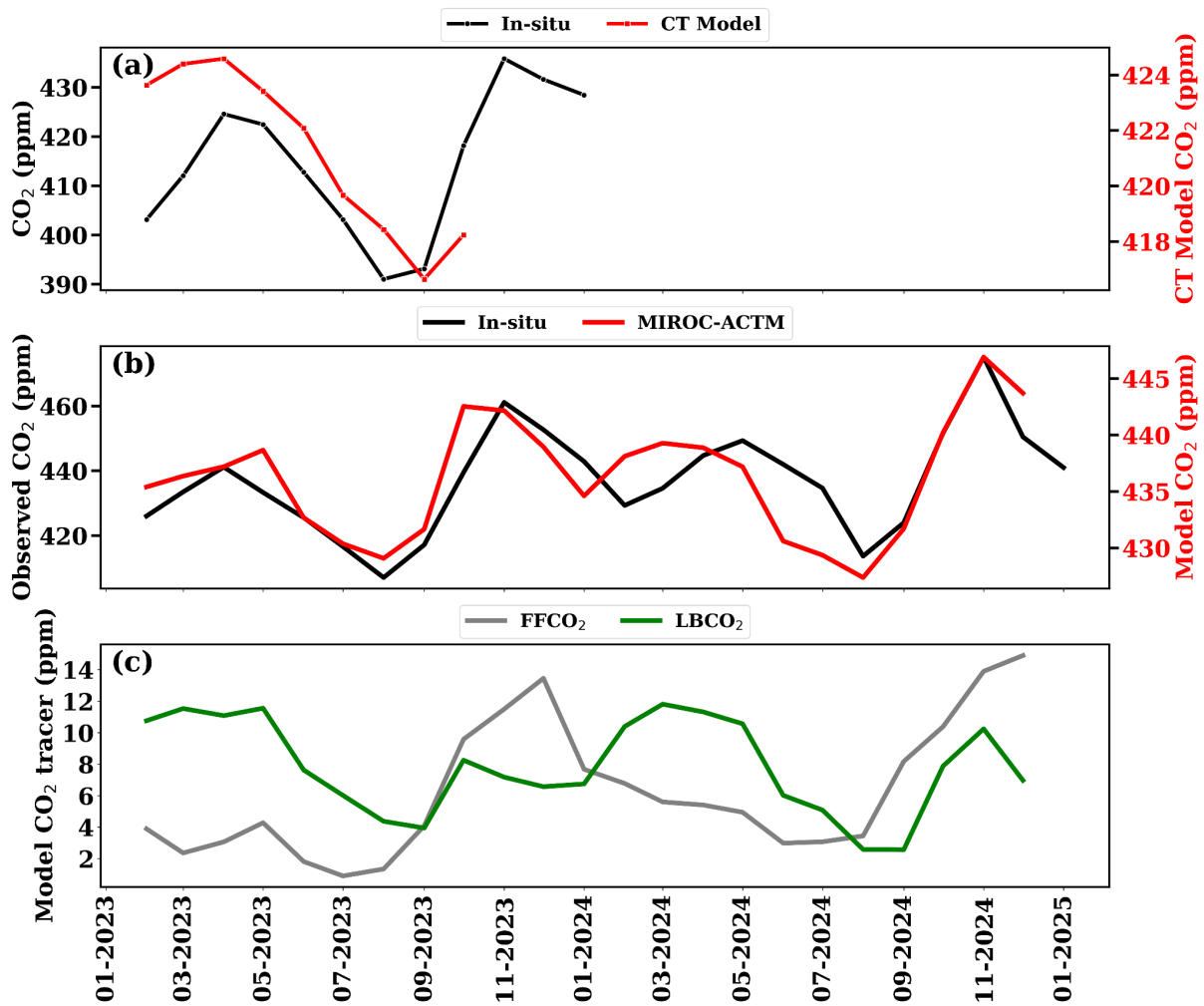
321 **Figure 3:** (a) Monthly variations of atmospheric CO₂ mole fraction (black) and PBLH (blue)
 322 and (b) NDVI (green) and SIF (orange) over the Sonipat monitoring station during the study
 323 period. The shaded background represents different seasons; yellow (pre-monsoon), green
 324 (monsoon), red (post-monsoon) and blue (winter).

325 The seasonal change in CO₂ was examined using two different vegetation indices
 326 (normalised difference vegetation index, NDVI and solar-induced fluorescence, SIF) to assess
 327 the role of the biosphere in CO₂ mole fractions over Sonipat. Both NDVI and SIF have been
 328 widely used as indicators of vegetation cover and photosynthetic activity (Aburas et al., 2015;
 329 Nath, 2014). Our analysis shows a strong inverse relationship between CO₂ levels and NDVI,
 330 as illustrated in Figure 3b. A noticeable decrease in atmospheric CO₂ mole fraction is observed
 331 at the onset of the monsoon (June), with increased vegetative activity continuing until
 332 September. Increased vegetation cover increases photosynthetic carbon uptake by the
 333 biosphere. However, as vegetation activity decreases from the post-monsoon to winter and pre-
 334 monsoon seasons, photosynthetic carbon uptake decreases, leading to a rise in atmospheric
 335 CO₂. Spearman's rank correlation analysis showed a weak and statistically insignificant
 336 relationship between CO₂ and NDVI ($\rho = -0.09$, $p = 0.74$). In contrast, CO₂ exhibited a
 337 moderate negative correlation with SIF ($\rho = -0.42$, $p = 0.07$). The negative correlation with
 338 SIF is consistent with enhanced biospheric uptake during periods of increased photosynthetic
 339 activity. Similar studies (Metya et al., 2021; Sreenivas et al., 2016; Tiwari et al., 2014), over
 340 India exhibited a strong dependence of CO₂ seasonality on local vegetative carbon uptake.

341 A sharp decrease in the seasonal mean (~18 ppm) was noted from pre-monsoon to
342 monsoon, attributed to enhanced photosynthetic activity around the measurement site, driven
343 by abundant soil moisture. A further decrease in CO₂ mole fraction is also observed as the
344 monsoon progresses, with minimum CO₂ mole fractions observed in August. The decreases in
345 temperature (due to cloudy, overcast conditions prevailing during these months) reduce leaf
346 and soil respiration, thereby enhancing carbon uptake (Jing et al., 2010; Patil et al., 2014).
347 Further, an increase in CO₂ mole fraction (~34 ppm) is observed during post-monsoon,
348 reflecting higher ecosystem respiration (Sharma et al., 2014) and enhanced soil microbial
349 activity (Fan & Forkel, 2025; Munksgaard et al., 2022), particularly from nocturnal respiration
350 prior to crop harvest. The gradual decline in NDVI during this period indicates reduced CO₂
351 uptake by vegetation. This season coincided with crop-burning episodes in northern India,
352 which significantly increased CO₂ mole fractions. A sharp decrease (~16 ppm) in the seasonal
353 mean during winter is evident compared to the post-monsoon. The shallow PBLH and winds
354 from western IGP that transport crop-burning residue contribute to the enhanced mole fraction
355 during winter. Table S2 compares the seasonal amplitude and the peak and drawdown months
356 at the measurement site with those in similar studies across India. Sonipat exhibits higher
357 seasonal amplitudes than other sites. However, a similar pattern in CO₂ peak and drawdown
358 months is evident in other monitoring stations.

359 **3.2.2 Seasonal constraints from model and satellites**

360 Figure 4(a) shows the comparison of ground-based mole fraction of CO₂ with CarbonTracker
361 inverse model (CT2022) simulated mole fraction (see different y-axis). The model outputs
362 beyond October 2023 were not publicly available. In general, the CT2022 model-simulated
363 mole fractions are much lower than the observed mole fractions at the Sonipat station. The
364 discrepancy is mainly due to the model's coarser resolution. Nevertheless, the model-simulated
365 seasonal pattern of CO₂ mole fraction is broadly in agreement with observations (Figure 4).
366 The CT2022 model simulates a minimum mole fraction of 416 ppm in September, whereas in
367 situ measurements show a minimum of 407 ppm in August. The CT2022 model exhibits higher
368 mole fractions during the pre-monsoon season, consistent with in situ data. Note that most
369 global and regional chemical transport models were unable to reproduce the large seasonal
370 amplitude of surface-based measured atmospheric CO₂ mole fractions at any of the monitoring
371 stations in India with different ecosystems (Lin et al., 2018; Philip et al., 2022).

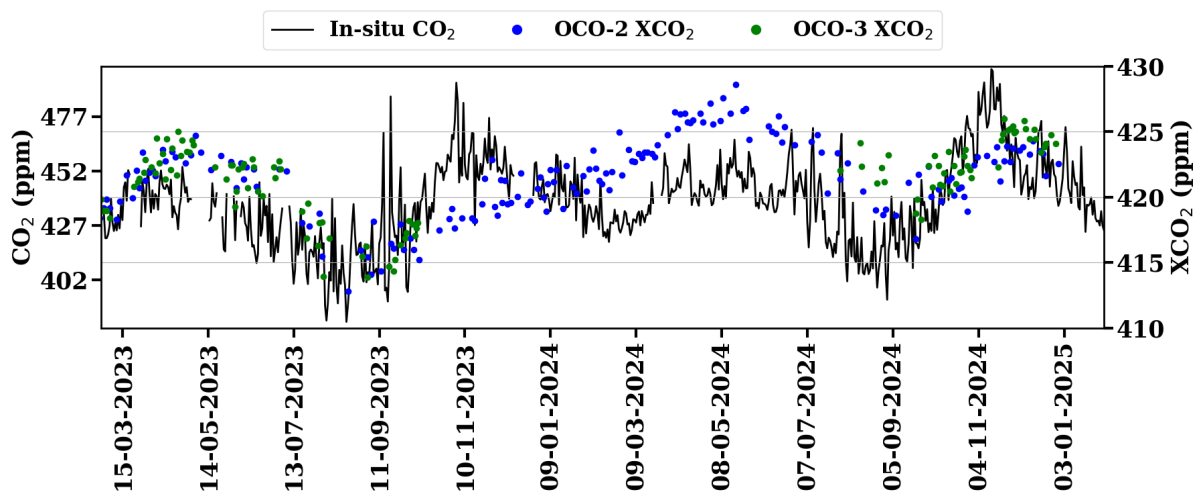


372
 373 **Figure 4:** (a) Monthly mean background CO₂ mole fraction over Sonipat (estimated using the
 374 ADVS method) compared to CarbonTracker (CT2022) model-simulated values at daytime
 375 (13:00 – 16:00). Note that the left y-axis represents surface mole fraction from in situ
 376 measurements, and the right y-axis represents CT2022-simulated mole fraction. (b) comparison
 377 of simulated mole fraction of atmospheric CO₂ from MIROC-ACTM with in situ
 378 measurements at Sonipat and (c) monthly averaged time series of different tracers from the
 379 MIROC-ACTM.

380

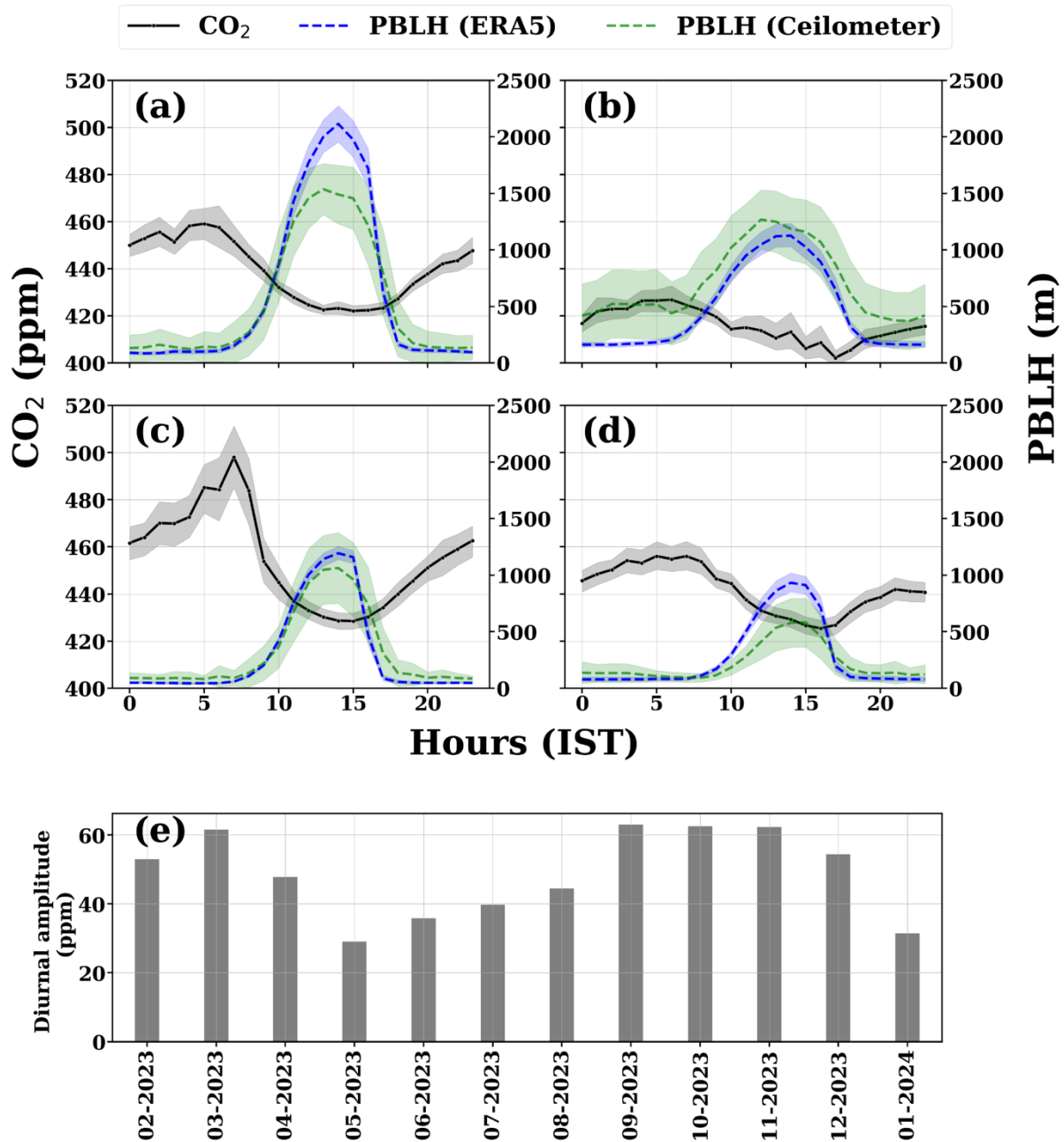
381 Figure 4(b) shows the comparison of atmospheric CO₂ mole fractions over Sonipat with
 382 the simulated mole fraction of CO₂ from the MIROC4-ACTM model. Similar to CT2022,
 383 MIROC captures the seasonal pattern of CO₂, but fails to capture the actual seasonal amplitude
 384 over Sonipat. Figure 4(c) presents the monthly averaged time series of model-simulated CO₂
 385 tracers. The fossil fuel tracer (FFCO₂) exhibits a peak in the post-monsoon period, followed by
 386 a gradual decrease through the end of winter. The shallow PBLH during this time traps
 387 vehicular emissions from NH-44 and industrial sources upwind of the monitoring station,

388 resulting in higher FFCO₂. With the development of the PBLH in the pre-monsoon, FFCO₂
 389 shows a gradual decrease, and rainfall during the monsoon results in minimum values during
 390 this time. The biospheric tracer (LBCO₂) shows a peak during the pre-monsoon, driven by dry
 391 soil conditions and a lack of vegetation and a drawdown during the monsoon. A sharp increase
 392 in LBCO₂ is observed during the post-monsoon season, coinciding with the harvest period at
 393 the monitoring station. Being surrounded by agricultural land, Sonipat is prone to emissions
 394 from crop residue burning around and upwind of the monitoring station. Both models
 395 underestimate these enhancements from regional sources.



396
 397 **Figure 5:** Daily variations of atmospheric CO₂ mole fraction from in situ measurements over
 398 Sonipat (left y-axis) with column average CO₂ mole fraction (XCO₂) from the OCO-2 (ppm)
 399 and OCO-3 (ppm) satellite instruments (right y-axis).

400
 401 Figure 5 compares XCO₂ from OCO-2 and OCO-3 satellites with ground-based CO₂
 402 measurements at Sonipat during the study period. XCO₂ reveals a similar seasonal pattern with
 403 high mole fraction during the pre-monsoon season, followed by a drawdown in CO₂ mole
 404 fraction during the monsoon season and a further gradual increase in CO₂ during the post-
 405 monsoon and winter. Although the satellite column data captures the monthly variability
 406 reasonably well, it fails to capture the sharp increase in mole fraction during the post-monsoon.
 407 This post-monsoon enhancement from crop residue burning at the monitoring station, along
 408 with additional transport from Punjab, highlights the limitations of high-resolution satellite data
 409 in capturing local enhancements.



410
 411 **Figure 6:** (a-d) Seasonally-averaged diurnal variation of atmospheric CO₂ over the Sonipat
 412 station during the pre-monsoon (MAM), monsoon (JJAS), post-monsoon (ON) and winter
 413 (DJF) seasons with planetary boundary layer heights (blue denotes PBLH from ERA5 and
 414 green denotes PBLH derived from Ceilometer), (e) monthly variation of the diurnal amplitude
 415 of CO₂ from February 2023 to January 2024.

416

417 3.3 Diurnal variability

418 Figure 6 (a-d) presents the averaged diurnal variation of atmospheric CO₂ mole
 419 fractions along with PBLH from ERA5 and Ceilometer at Sonipat during four seasons for the

420 first year of the study (February 2023 – January 2024). Figure S5 presents the diurnal variation
421 for the second year of the study. The diurnal cycle has been analysed separately for each year,
422 combining available PBLH data. All seasons exhibit a similar diurnal pattern, with maximum
423 CO₂ mole fractions in the early morning hours (05:00 - 08:00 am) and minimum mole fractions
424 in the late afternoon hours (2:00 - 3:00 pm). The observed diurnal cycle of CO₂ is closely
425 associated with the development of PBLH during the day (Figure 6). The peak in CO₂ mole
426 fraction during the morning hours can be attributed to the fumigation effect, and a well-mixed
427 PBL dilutes CO₂ mole fractions during the afternoon hours.

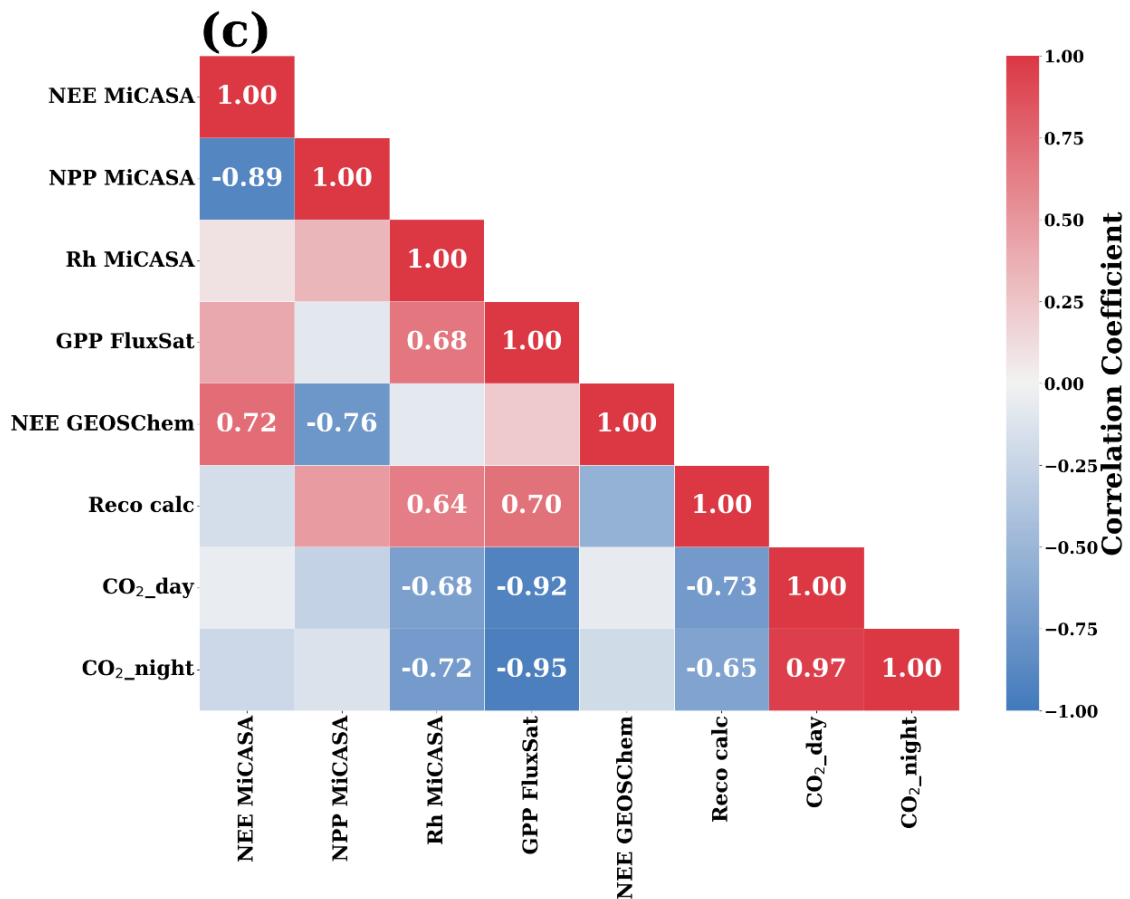
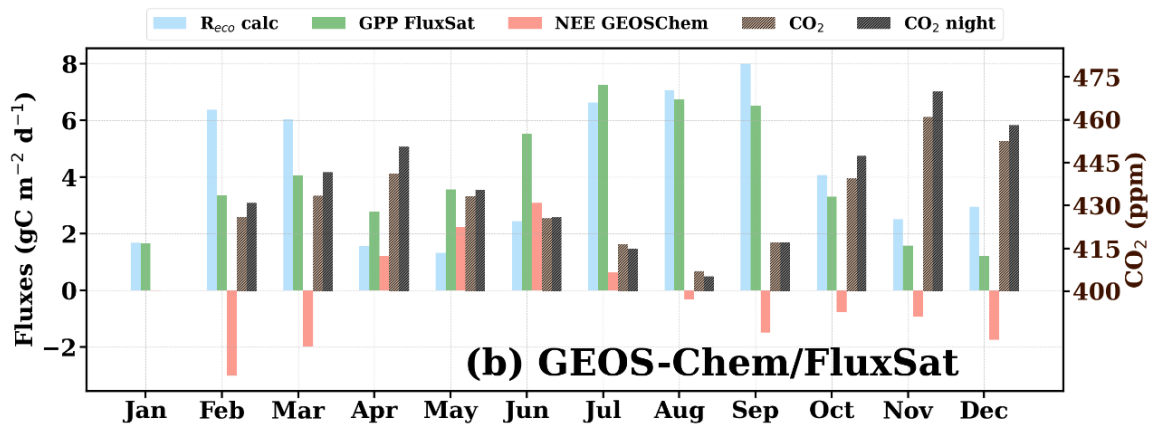
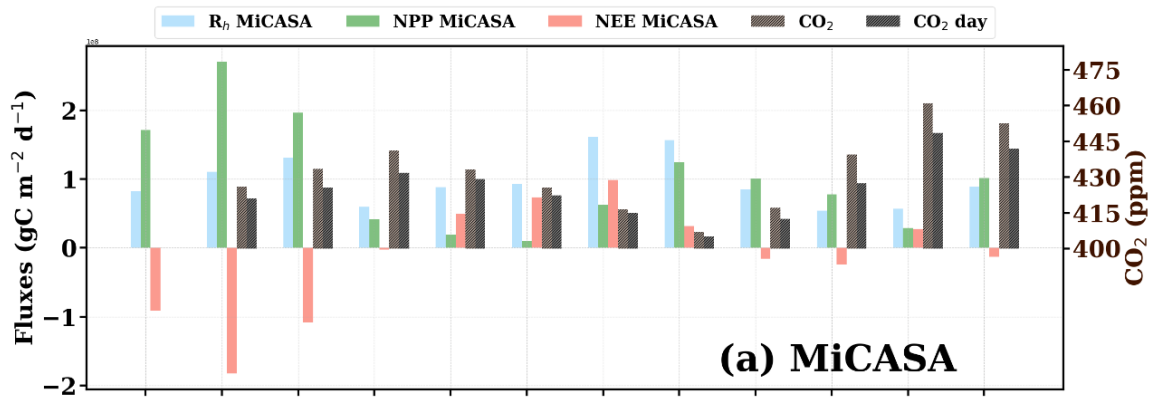
428 Photosynthetic activity is another key driver of diurnal variability at Sonipat, a
429 characteristic observed in rural areas with vegetative cover (Imasu & Tanabe, 2018). Strong
430 vegetative uptake of CO₂ during the monsoon results in minimum daytime CO₂ mole fractions,
431 and the lack of vegetation during post-monsoon contributes to maximum daytime CO₂ mole
432 fractions during this season. The diurnal variation of GHGs reported by several studies
433 (Nishanth et al., 2014; Patil et al., 2014; Sharma et al., 2014) from different parts of the country
434 shows a similar trend. The same was observed for 2024 as well (Figure S5). The diurnal
435 variability of CO₂ over Sonipat is driven by biospheric activity and local meteorology.

436 Figure 6(e) shows the monthly average variation in diurnal amplitude (difference between the
437 maximum and minimum mole fraction of CO₂ in the diurnal cycle) during the first year. The
438 lowest diurnal amplitude of about 29 ppm is observed in May, while the highest amplitude at
439 about 63 ppm is observed in September/October. We found that the post-monsoon season
440 exhibited the highest diurnal variability (~60 ppm), followed by the pre-monsoon (~35 ppm),
441 winter (~30 ppm), and monsoon (~20 ppm) seasons.

442

443 **3.4 Drivers of CO₂ seasonality**

444 The contribution of biospheric fluxes in driving the CO₂ mole fraction over Sonipat (for
445 2023) was analysed in Figure 7. Figure 7(a) shows the simulated data from the Mi CASA
446 biosphere model along with the monthly averaged mole fractions of CO₂ and daytime CO₂
447 (06:00 – 18:00). Figure 7(b) presents the simulated NEE from GEOS-Chem and GPP from
448 FluxSat, along with the monthly averaged mole fractions of daily-mean and nighttime CO₂
449 (18:00 – 06:00). Positive NEE values indicate a net exchange of CO₂ from the biosphere to the
450 atmosphere. On the other hand, a negative NEE value (when NPP exceeds Rh) suggests the
451 uptake of CO₂ from the atmosphere to the biosphere.



453 **Figure 7:** Monthly variation of atmospheric CO₂ mole fraction (for 2023) over the Sonipat
454 monitoring station compared against (a) biospheric fluxes from the MiCASA terrestrial
455 biospheric model and (b) GEOS-Chem model and FluxSat GPP data. (a - b) The CO₂ mole
456 fraction are daytime-mean (06:00 - 18:00 LT) and night time-mean (18:00 - 06:00 LT). The
457 correlation heatmap of all the variables. The annual growth rate of CO₂ has been subtracted
458 from the CO₂ mole fraction using background data from the Mauna Lou observatory. The
459 variable “Reco calc” was calculated as the difference between NEE (GEOS-Chem) and GPP
460 (FluxSat). The Pearson correlation coefficients with a p value less than 0.05 have been
461 displayed in the correlation plot.

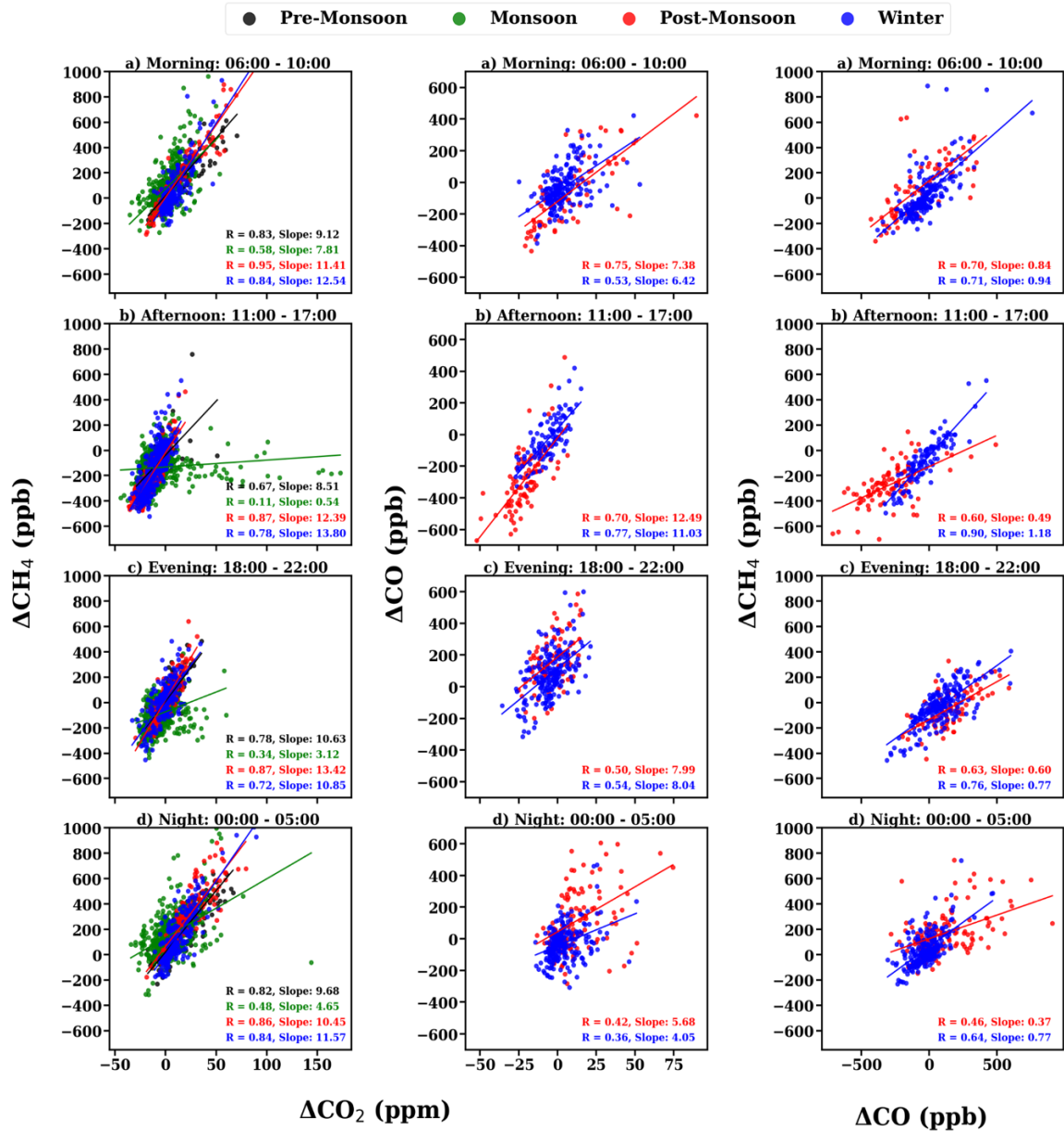
462

463 The NEE flux shows a strong positive in June, followed by a gradual decrease through
464 October (monsoon). During this time, Reco, Rh and GPP exhibit strong enhancements. These
465 enhancements are accompanied by a drawdown of CO₂ during this time. The driving factor
466 behind this CO₂ drawdown during monsoon is the enhanced ecosystem productivity during this
467 time. Strong inverse correlations of GPP, Rh, and Reco with CO₂ suggested that the biosphere
468 acts as a net sink of CO₂ (Figure 8c).

469 Interestingly, post-monsoon and winter months exhibit weak or negative NEE. This is
470 because Rh values are low during these seasons due to drier soil conditions and lower soil
471 moisture. It is also notable that GPP is very low during these months, which is associated with
472 a high CO₂ mole fraction. Significant contributions of air-mass transport from upwind regions
473 and boundary-layer dynamics, along with the lack of vegetation during this time, contribute to
474 the buildup of CO₂ mole fraction.

475

476



477

478 **Figure 8:** Tracer-tracer relations of $\Delta\text{CO}_2 / \Delta\text{CH}_4$ (left panel), $\Delta\text{CO}_2 / \Delta\text{CO}$ (middle panel) and
 479 $\Delta\text{CH}_4 / \Delta\text{CO}$ (right panel) during a) Morning (0600–1000 IST), b) afternoon (1100–1700 IST),
 480 c) evening (1800–2200 IST) and d) night (0000–0500 IST).

481

482 3.5 Emission source detection using tracer-tracer relationships

483 The ratios (tracer-tracer) of GHGs have been widely used in previous studies to estimate
 484 different emission source contributions to atmospheric GHGs (Chandra et al., 2016, 2019; Lin
 485 et al., 2015; Lopez, 2012; Paris et al., 2008; Sreenivas et al., 2016, 2022). We followed a similar
 486 tracer-tracer correlation analysis to assess synoptic variation in CO₂ across different diurnal
 487 time windows and understand the emission sources contributing to CO₂ mole fractions over

488 Sonipat (Figure 8). The measurements have been divided into four-time windows: (a) morning
489 hours (06:00 - 10:00; the PBLH starts to develop after sunrise; local traffic is high), (b)
490 afternoon hours (11:00 - 17:00; the PBLH is well-developed; relatively minimum local traffic,
491 (c) evening hours (18:00 - 22:00; rush hour traffic and high household emissions), and (d) night
492 hours (00:00 - 00:05; relatively less anthropogenic emission sources). Excess mole fractions
493 were used in the correlation analysis to remove the influence of background mole fractions on
494 the correlation ratios (Worthy et al., 2009). The correlation between the different gases (CO₂,
495 CH₄, and CO) has been studied using the robust linear fit regression method.

496

497 Figure 8 (left panel) presents the correlation of excess mole fraction of CH₄ and CO₂
498 during the four seasons. The CH₄/CO₂ correlation reveals a strong correlation ($r > 0.6$) for all
499 seasons except monsoon during all time windows, which suggests a similar source mechanism
500 or a controlling emission process for both gases at the measurement site. Around the monitoring
501 station, vehicular emissions from the nearby highway and natural gas combustion emissions
502 are possible sources. Also, a positive correlation suggests that anthropogenic emissions
503 dominate the carbon cycle in Sonipat (Fang et al., 2015). The regression slope shows strong
504 diurnal variation throughout all seasons. Recent studies across India have reported similar
505 results, with higher regression slopes during the post-monsoon and winter seasons than during
506 the pre-monsoon and monsoon seasons (Lin et al., 2015; Sreenivas et al., 2016, 2022).

507

508 Figure 8 (middle panel) presents the correlation of excess mole fractions of CO and
509 CO₂ during post-monsoon and winter. The CO/CO₂ ratio over Sonipat (4 – 12.5 ppb ppm⁻¹) is
510 lower than that for fresh plumes from wildfire (Andreae and Merlet, 2001; Mauzerall et al.,
511 1998) and much lower than that from biomass burning events alone (Matsueda et al., 1999).
512 Lin et al. (2015) reported CO/CO₂ ratios of 13 ppb ppm⁻¹ over Southeast Asian outflow from
513 February to April 2001. This value was found to be influenced by fossil fuel emissions (Russo
514 et al., 2003), crop residue burning, and biofuel burning rather than solely by biomass/biofuel
515 burning. The CO/CO₂ ratios over Sonipat during the post-monsoon and winter closely match
516 those of Lin et al. (2015), suggesting that the high CO₂ mole fractions during this time are an
517 interplay of different sources like crop residue burning (long-range transport) and other fossil-
518 fuel emissions (vehicular and industrial) around the monitoring station.

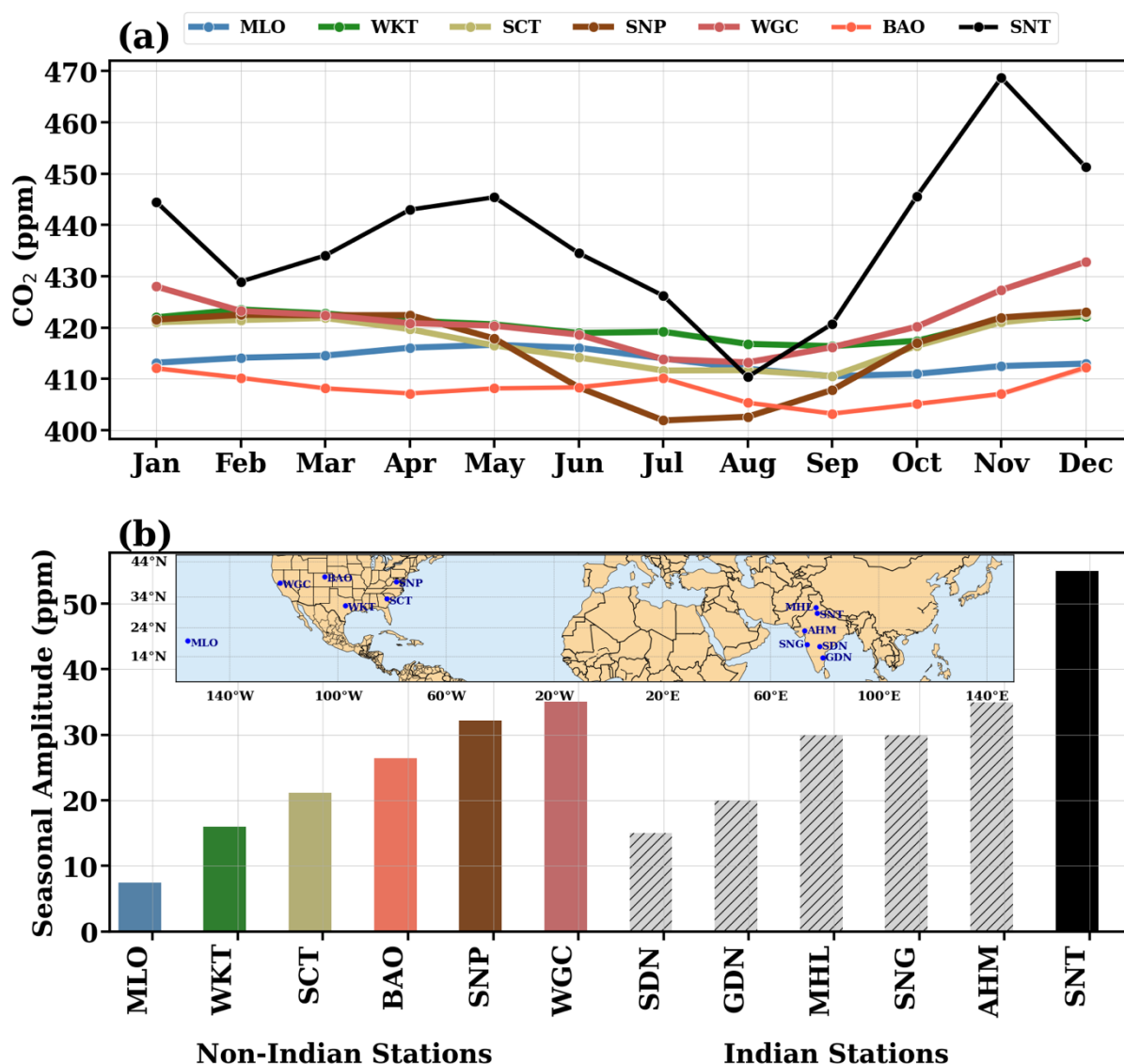
519

520 Figure 8 (right panel) presents the correlation of excess mole fractions of CH₄ and CO during
521 post-monsoon and winter. The CH₄/CO ratios range from 0.3 to 1.2 at Sonipat, indicative of

522 anthropogenic emission sources (Bakwin et al., 1995; Harriss et al., 1994; Lai et al., 2010; Lin
 523 et al., 2015; Niwa et al., 2012; Sawa et al., 2004; Wada et al., 2011; Xiao et al., 2004). In
 524 contrast, ratios influenced solely by biomass and biofuel burning are much lower, ranging from
 525 0.07 to 0.3 (Andreae and Merlet, 2001; Mauzerall et al., 1998; Mühle et al., 2002).

526 These lower ratios highlight the significant difference when compared to the values
 527 recorded in Sonipat. Moreover, very high CH₄ emissions from livestock can elevate the
 528 generally low CH₄/CO ratios associated with biomass burning. This indicates substantial
 529 contributions from various CH₄ sources apart from biofuel burning.

530



531 **Figure 9:** (a) Comparison of the seasonal variability of atmospheric CO₂ over Sonipat
 532 monitoring station with various locations in the same latitudinal band. (b) Comparison of the
 533 seasonal amplitude between Indian (coloured bars) and international monitoring stations (grey
 534 bars). Indian stations include Shadnagar (SDN), Sinhadgad (SNG), Ahmedabad (AHM), Mohali
 535 bars).

536 (MHL), Gadanki (GDN), and Sonipat (SNT). International stations include Mauna Loa (MLO),
537 South Carolina (SCT), Shenandoah National Park (SNP), Walnut Grove, (WGC), Moody
538 (WKT) and Boulder (BAO). For all international stations except BAO, the five-year average
539 (2018 - 2022) has been chosen for the seasonality. For BAO, 2011 – 2016 has been used due
540 to lack of coinciding data. The monthly average of the entire study period (February 2023 –
541 January 2025) has been used for this comparison.

542

543 **4. Discussions**

544 By investigating two years of high-frequency atmospheric CO₂ mole fraction measurements at
545 the Sonipat station in the IGP region, we identified the following salient features about the
546 seasonality, diurnal variability, drivers of temporal variability, and emission sources of CO₂.

547 **Very high atmospheric CO₂ mole fractions over IGP:** The surface-based
548 measurements of atmospheric CO₂ mole fraction exhibit strong seasonality, with a maximum
549 (456.4 ppm) during post-monsoon and a minimum (407.2 ppm) during monsoon, with an
550 average of 422.6 ppm. Seasonal changes in the PBLH affected the atmospheric CO₂ mole
551 fraction by diluting or concentrating GHG mole fractions near the surface. A strong dependence
552 of CO₂ seasonality on local vegetative carbon uptake was observed from the negative
553 correlation between NDVI and CO₂ mole fractions, which was consistent across India (Metya
554 et al., 2021; Sreenivas et al., 2016; Tiwari et al., 2014).

555 A comparison of the seasonality of atmospheric CO₂ at Sonipat with other Indian and
556 global sites in the same latitudinal band revealed very high seasonality at Sonipat, surpassing
557 that of all other stations. This high seasonality is attributed to elevated CO₂ mole fractions in
558 November (post-monsoon), driven by local emissions and crop residue burning. Figure 9a
559 presents the monthly averaged variation of CO₂ over Sonipat during the study period (SNT)
560 with other measurement sites in the same latitudinal band (5° N – 40° N). Details of all
561 monitoring stations used in this study are described in detail in S1. Sonipat exhibits a very high
562 seasonal amplitude (~60 ppm) compared to other sites worldwide (~15 ppm, see Figure 9b),
563 attributed to the sharp increase in post-monsoon, consistent in both years of the study (see
564 Figure 2). Excluding November would reduce the seasonal amplitude of Sonipat to 35 ppm,
565 which is comparable to that in Ahmedabad (35 ppm). Temperature-driven PBLH (which
566 inhibits mixing) and strong north-westerly winds (which induce transport of emissions from
567 upwind) during this season play a key role in these high CO₂ mole fractions (Figure S3 and

568 S4). It is also noted that the CO₂ drawdown in August is primarily due to the green paddy fields
569 during the monsoon (terrestrial CO₂ uptake), coinciding with heavy rains that wash out CO₂.
570 This combined effect makes the lowest CO₂ mole fractions in Sonipat comparable to those at
571 some background stations across the globe with different ecosystems (Figure 9a).

572 This study also analysed the drivers of this variability using various ecosystem variables,
573 including NEE, which represents the net carbon exchange between terrestrial ecosystems (the
574 difference between Rh and NPP). NPP is the net amount of CO₂ retained in the biosphere. Rh
575 is the amount of CO₂ emitted into the atmosphere due to the decomposition of organic matter
576 by microorganisms in the soil. Reco, the sum of Ra (autotrophic respiration) and Rh has been
577 calculated as the difference of FluxSat GPP and GEOS-Chem NEE. GPP, a measure of carbon
578 uptake by plants, was observed to be very high during monsoon along with NEE, Rh and Reco.
579 Statistical analysis revealed a strong negative correlation of GPP with CO₂ and a strong positive
580 correlation with Rh and Reco. These suggest that the primary sink of CO₂ over Sonipat is
581 biospheric activity, driven by the abundance of vegetation resulting from enhanced soil
582 moisture during the monsoon.

583 **Performance of models and satellites over IGP:** Although both the CarbonTracker
584 and MIROC-ACTM models captured the broad seasonal pattern of CO₂ mole fractions, they
585 substantially underestimated it. However, MIROC showed greater seasonal variability than
586 CT2022, with post-monsoon highs and pre-monsoon drawdowns showing strong correlations
587 with in situ measurements. Further analysis of the tracers from MIROC provides insights into
588 the driving factors of this variability. The post-monsoon peak is attributed to vehicular
589 emissions from the nearby highway and industrial sources upwind of the monitoring station.
590 The drawdown in monsoon is attributed to the added soil moisture and increased CO₂ uptake
591 by plants during this time. The location of the measurement site in IGP, downwind of Punjab,
592 provides insights into this transport-induced enhancement. The OCO-2 and OCO-3 satellite
593 XCO₂ retrievals also showed similar seasonal variability; however, the satellites could not
594 capture CO₂ enhancements from local sources.

595 **Diurnal variability driven by meteorology:** The atmospheric CO₂ mole fraction at
596 Sonipat exhibits a consistent diurnal pattern across seasons. It was observed that CO₂ mole
597 fractions steadily increased throughout the night, reaching a peak in the early morning hours.
598 This accumulation of CO₂ during the night-time can be attributed to the fumigation effect: a
599 significant rise in surface mole fractions, notable during the early morning hours due to the

600 breakdown of the nocturnal inversion layer following sunrise (Stull, 1988). Weak winds and
601 shallow PBLH enhance the fumigation effect. The combined effect of photosynthetic activity
602 and mixing of PBLH during the afternoon hours drives the CO₂ mole fractions during different
603 seasons. The diurnal amplitude shows large month-to-month variation with an increasing trend
604 from May to September 2023 and a decreasing trend till February 2024. Figure S6 presents the
605 seasonal variation of CO₂ compared with PBLH derived from Ceilometer and ERA5 reanalysis
606 data for 2023. A slight shift in the timing of the morning peaks was observed from season to
607 season, due to changes in sunrise time, which affected photosynthetic activity.

608 **Detecting emission source contributions:** Tracer-tracer relationships across different
609 time periods during the post-monsoon and winter seasons were examined. Analysis reveals
610 that CO₂ and CH₄ exhibit a strong positive correlation across all seasons, suggesting common
611 sources for both gases. During monsoon season, the afternoon time window shows a weak
612 correlation with other time windows, revealing distinct source and sink mechanisms for CO₂
613 and CH₄, such as CH₄ loss via hydroxyl radical and CO₂ uptake by plants. The regression
614 slope is higher during the post-monsoon and winter months, when reduced photosynthetic
615 activity and the dominance of local emissions and long-range transport are observed. The
616 lower values during pre-monsoon and monsoon are associated with the dominance of
617 vegetation and terrestrial uptake of CO₂ by photosynthetic activity.

618 The CO/CO₂ correlation shows strong diurnal variability, suggesting the dominance of
619 different source mechanisms throughout the day, with strong correlation during the morning
620 and afternoon hours (suggesting a similar source) and weaker correlation during the evening
621 and night hours (suggesting different sources). The post-monsoon season shows higher
622 regression slopes due to reduced photosynthetic activity. Over Sonipat, the contribution of CO
623 and CO₂ from long-range air mass transport (influenced by crop residue burning in Punjab)
624 during post-monsoon from the northwest of the monitoring station is diluted by other sources
625 (such as vehicular emissions from highways, crop residue burning, and open burning). The
626 contribution of biofuel burning (which has a higher burning efficiency) during post-monsoon
627 and winter (Andreae and Merlet, 2001) can also reduce the CO/CO₂ ratios. Figure S4 presents
628 the wind patterns during the different seasons, revealing the predominant winds from the
629 northwest during the post-monsoon season. The CO/CO₂ ratios reveal the combined influence
630 of various sources around and upwind of the monitoring station during the post-monsoon
631 period.

632 The CH₄/CO correlation ($r > 0.7$) was stronger during winter than during post-monsoon
633 across all time windows, suggesting similar sources during winter and different sources during
634 post-monsoon. The regression slope was higher during winter than during the post-monsoon
635 period. This was traced to the lack of photosynthetic activity and the dominance of local
636 emissions and long-range transport. Lin et al. (2015) reported comparable CH₄/CO ratios at
637 Pondicherry (PON) and Port Blair (PBL). CH₄ and CO emissions from biomass, biofuel
638 burning and livestock estimated from EDGAR v4.2, 2011 indicate a CH₄/CO ratio of 0.64 –
639 0.69 over the Indian subcontinent from 2000-2008. These ratios are comparable to those
640 observed during both seasons at Sonipat.

641 In summary, this study demonstrated that this high temporal CO₂ variability across the
642 IGP region arises from an interplay of local anthropogenic and biomass-burning emissions,
643 biospheric fluxes, and prevailing meteorology.

644

645 **5. Conclusions**

646 In this study, we conducted high frequency measurements of atmospheric CO₂ mole fractions
647 at a suburban station in the Indo-Gangetic Plain, Sonipat and investigated the carbon cycle
648 dynamics over IGP. The atmospheric CO₂ mole fractions from February 2023 to January 2025
649 have been measured using a GHG analyser with laser-based cavity ring-down spectroscopy.
650 CO₂ molefractions over Sonipat recorded an annual average of 440.8 ± 19.7 parts per million
651 (ppm) in 2024, with a very high seasonal variability of ~ 60 ppm, much higher than that of other
652 monitoring stations in the same latitudnal band. Post-monsoon recorded the highest diurnal
653 variability (~ 60 ppm) and monsoon recorded the least (~ 20 ppm) with a consistent diurnal
654 pattern irrespective of season. By examining a series of observational and modelling data, such
655 as ground-based and satellite-based measurements, three model outputs, ecosystem proxy
656 variables, and the tracer-tracer analysis technique, we identified the drivers of the high temporal
657 variability of CO₂ over Sonipat and the IGP region. First, this high seasonality is attributed to
658 elevated CO₂ mole fractions in November (post-monsoon), driven by local emissions and crop
659 residue burning. We found that biospheric activity was the primary driver of seasonal changes
660 over Sonipat, with anthropogenic emissions and soil respiration as the major sources and
661 photosynthetic carbon uptake as the major sink. In addition, boundary-layer dynamics and air-
662 mass transport from upwind regions significantly contribute to the buildup of CO₂ mole
663 fraction. Second, we found that although both the CarbonTracker and MIROC-ACTM models
664 captured the broad seasonal pattern of CO₂ mole fractions, they substantially underestimated
665 it. Moreover, the OCO-2 and OCO-3 satellite XCO₂ retrievals also showed similar seasonal

666 variability; however, the satellites could not capture CO₂ enhancements from local sources.
667 Third, we found that the atmospheric CO₂ mole fraction at Sonipat exhibits a consistent diurnal
668 pattern irrespective of season, with a maximum during the morning hours, attributed to the
669 fumigation effect, followed by a gradual decrease during the day and a minimum during the
670 afternoon hours, when photosynthetic activity is enhanced. Finally, tracer-tracer relationships
671 across different time periods in the post-monsoon and winter seasons revealed common sources
672 of CO₂ and CH₄. The CO/CO₂ ratios reveal the combined influence of vehicular emissions,
673 crop residue burning, and open burning on CO₂ mole fractions in Sonipat during the post-
674 monsoon period. This study identified key sources and drivers of the high CO₂ temporal
675 variability in a data-sparse IGP region. These findings advance our understanding of carbon
676 cycle dynamics, with direct implications for mitigation and policy.

677 **Data availability**

- 678 ● The observational datasets used in this study are publicly available in a Zenodo
679 archive and can be accessed from [10.5281/zenodo.1962872](https://zenodo.org/record/1962872)
- 680 ● The OCO-2 and OCO-3 data is downloaded from <https://disc.gsfc.nasa.gov/datasets/>.
681 This study utilizes the bias-corrected OCO-2 v11.1r data product
682 ([https://disc.gsfc.nasa.gov/datasets/OCO2_L2_Lite_FP_11.1r/summary?keywords=oc](https://disc.gsfc.nasa.gov/datasets/OCO2_L2_Lite_FP_11.1r/summary?keywords=oco2)
683 [o2](https://disc.gsfc.nasa.gov/datasets/OCO2_L2_Lite_FP_11.1r/summary?keywords=oco2)) and the OCO-3 v10.4r data product
684 ([https://disc.gsfc.nasa.gov/datasets/OCO3_L2_Lite_FP_10.4r/summary?keywords=oc](https://disc.gsfc.nasa.gov/datasets/OCO3_L2_Lite_FP_10.4r/summary?keywords=oco3)
685 [o3](https://disc.gsfc.nasa.gov/datasets/OCO3_L2_Lite_FP_10.4r/summary?keywords=oco3)).
- 686 ● The CT-2020 model outputs were downloaded from
687 <https://gml.noaa.gov/aftp/products/carbontracker/co2/>. The CASA model outputs
688 were downloaded from
689 [https://disc.gsfc.nasa.gov/datasets/GEOS_CASAGFED_M_FLUX_3/summary?keyw](https://disc.gsfc.nasa.gov/datasets/GEOS_CASAGFED_M_FLUX_3/summary?keywords=CASA)
690 [ords=CASA](https://disc.gsfc.nasa.gov/datasets/GEOS_CASAGFED_M_FLUX_3/summary?keywords=CASA).
- 691 ● The ERA5 reanalysis datasets were downloaded from
692 <https://cds.climate.copernicus.eu/cdsapp#!/dataset/reanalysis-era5-single-levels>.
- 693 ● The satellite estimates of NDVI were downloaded from
694 <https://www.ncei.noaa.gov/data/land-normalized-difference-vegetation-index/access/>.
- 695 ● This study utilises bias-corrected SIF data from OCO-2 v11r data product
696 ([https://disc.gsfc.nasa.gov/datasets/OCO2_L2_Lite_SIF_11r/summary?keywords=oco](https://disc.gsfc.nasa.gov/datasets/OCO2_L2_Lite_SIF_11r/summary?keywords=oco2%20sif)
697 [2%20sif](https://disc.gsfc.nasa.gov/datasets/OCO2_L2_Lite_SIF_11r/summary?keywords=oco2%20sif)).

- 698 • The FluxSat data is downloaded from
699 https://avdc.gsfc.nasa.gov/pub/tmp/FluxSat_GPP/. This study uses FluxSat version
700 2.2 dataproduct.
701 • The ObsPack data is available at <https://gml.noaa.gov/ccgg/obspace/data.php>. This
702 study used ObsPack V2.0 dataproduct.
703

704

Acknowledgements:

705 We acknowledge institutional support and funding provided by IIT Delhi and other
706 stakeholders to develop the IIT Delhi Atmospheric Observatory at Sonipat. In particular, we
707 thank Shahzad Gani (IIT Delhi) for his contribution to the observatory. We thank the Aakash
708 Project team for providing trace gas data from the CUPI-G sensors. We acknowledge the OCO-
709 2, OCO-3, CASA, CarbonTracker, and ERA5 teams for providing the data used in this study.
710

711

712

Author Contributions:

713 **Conceptualization:** VJV, RKK, SP

714 **Data curation:** VJV, RKK, JR, DG, SD, TN, YM, PKP

715 **Investigation, Methodology:** VJV, RKK, SP, PKP

716 **Software, Visualisation:** VJV

717 **Writing – original draft:** VJV

718 **Writing – review & editing:** RKK, SP, JR, DG, SD, YM, PKP

719

Competing interests

721 The authors declare that they have no conflict of interest.

722 **References**

- 723 Aburas, M. M., Abdullah, S. H., Ramli, M. F., and Ash'aari, Z. H.: Measuring Land Cover
724 Change in Seremban, Malaysia Using NDVI Index, *Procedia Environmental Sciences*, 30,
725 238–243, <https://doi.org/10.1016/j.proenv.2015.10.043>, 2015.
- 726 Ammoura, L., Xueref-Remy, I., Gros, V., Baudic, A., Bonsang, B., Petit, J.-E., Perrussel, O.,
727 Bonnaire, N., Sciare, J., and Chevallier, F.: Atmospheric measurements of ratios between
728 CO₂ and co-emitted species from traffic: a tunnel study in the Paris
729 megacity, *Atmos. Chem. Phys.*, 14, 12871–12882, [https://doi.org/10.5194/acp-14-12871-](https://doi.org/10.5194/acp-14-12871-2014)
730 2014, 2014.
- 731 Andreae, M. O. and Merlet, P.: Emission of trace gases and aerosols from biomass burning,
732 *Global Biogeochemical Cycles*, 15, 955–966, <https://doi.org/10.1029/2000GB001382>, 2001.
- 733 Apadula, F., Cassardo, C., Ferrarese, S., Heltai, D., and Lanza, A.: Thirty Years of
734 Atmospheric CO₂ Observations at the Plateau Rosa Station, Italy, *Atmosphere*, 10, 418,
735 <https://doi.org/10.3390/atmos10070418>, 2019.
- 736 Baars, H., Ansmann, A., Engelmann, R., and Althausen, D.: Continuous monitoring of the
737 boundary-layer top with lidar, *Atmospheric Chemistry and Physics*, 8, 7281–7296,
738 <https://doi.org/10.5194/acp-8-7281-2008>, 2008.
- 739 Baker, A. K., Schuck, T. J., Brenninkmeijer, C. A. M., Rauthe-Schöch, A., Slemr, F., van
740 Velthoven, P. F. J., and Lelieveld, J.: Estimating the contribution of monsoon-related
741 biogenic production to methane emissions from South Asia using CARIBIC observations,
742 *Geophysical Research Letters*, 39, <https://doi.org/10.1029/2012GL051756>, 2012.
- 743 Bakwin, P. S., Tans, P. S., Zhao, C., Ussler III, W., and Quesnell, E.: Measurements of
744 carbon dioxide on a very tall tower, *Tellus B: Chemical and Physical Meteorology*, 47, 535–
745 549, <https://doi.org/10.3402/tellusb.v47i5.16070>, 1995.
- 746 Bhattacharya, S. K., Borole, D. V., Francy, R. J., Allison, C. E., Steele, L. P., Krummel, P.,
747 Langenfelds, R., Masarie, K. A., Tiwari, Y. K., and Patra, P. K.: Trace gases and CO₂ isotope
748 records from Cabo de Rama, India, *Current Science*, 97, 1336–1344, 2009.
- 749 Bisht, J. S. H., Machida, T., Chandra, N., Tsuboi, K., Patra, P. K., Umezawa, T., Niwa, Y.,
750 Sawa, Y., Morimoto, S., Nakazawa, T., Saitoh, N., and Takigawa, M.: Seasonal Variations of
751 SF₆, CO₂, CH₄, and N₂O in the UT/LS Region due to Emissions, Transport, and Chemistry,
752 *JGR Atmospheres*, 126, e2020JD033541, <https://doi.org/10.1029/2020JD033541>, 2021.
- 753 Brad Weir (2024), MiCASA Daily NPP Rh Fire Fuel Fluxes 0.1 degree × 0.1 degree V1,
754 Greenbelt, MD, USA, NASA Center for Climate Simulation (NCCS) DataPortal, Accessed:
755 [March 20, 2025], 10.5067/ZBXSA1LEN453
- 756 Byrne, B., Jones, D. B. A., Strong, K., Zeng, Z. -C., Deng, F., and Liu, J.: Sensitivity of CO₂
757 surface flux constraints to observational coverage, *JGR Atmospheres*, 122, 6672–6694,
758 <https://doi.org/10.1002/2016JD026164>, 2017.
- 759 Chakraborty, S., Tiwari, Y. K., Deb Burman, P. K., Baidya Roy, S., and Valsala, V.:
760 Observations and Modeling of GHG Concentrations and Fluxes Over India, in: Assessment

761 of Climate Change over the Indian Region: A Report of the Ministry of Earth Sciences
762 (MoES), Government of India, edited by: Krishnan, R., Sanjay, J., Gnanaseelan, C.,
763 Mujumdar, M., Kulkarni, A., and Chakraborty, S., Springer, Singapore, 73–92,
764 https://doi.org/10.1007/978-981-15-4327-2_4, 2020.

765 Chandra, N., Lal, S., Venkataramani, S., Patra, P. K., and Sheel, V.: Temporal variations of
766 atmospheric CO₂ and CO at Ahmedabad in western India, *Atmos.*
767 *Chem. Phys.*, 16, 6153–6173, <https://doi.org/10.5194/acp-16-6153-2016>, 2016.

768 Chandra, N., Venkataramani, S., Lal, S., Patra, P. K., Ramonet, M., Lin, X., and Sharma, S.
769 K.: Observational evidence of high methane emissions over a city in western India,
770 *Atmospheric Environment*, 202, 41–52, <https://doi.org/10.1016/j.atmosenv.2019.01.007>,
771 2019.

772 Chandra, N., Patra, P. K., Bisht, J. S. H., Ito, A., Umezawa, T., Saigusa, N., Morimoto, S.,
773 Aoki, S., Janssens-Maenhout, G., Fujita, R., Takigawa, M., Watanabe, S., Saitoh, N., and
774 Canadell, J. G.: Emissions from the Oil and Gas Sectors, Coal Mining and Ruminant Farming
775 Drive Methane Growth over the Past Three Decades, *Journal of the Meteorological Society*
776 *of Japan*, 99, 309–337, <https://doi.org/10.2151/jmsj.2021-015>, 2021.

777 Chandra, N., Patra, P. K., Niwa, Y., Ito, A., Iida, Y., Goto, D., Morimoto, S., Kondo, M.,
778 Takigawa, M., Hajima, T., and Watanabe, M.: Estimated regional CO₂ flux and uncertainty
779 based on an ensemble of atmospheric CO₂ inversions, *Atmos. Chem. Phys.*, 22, 9215–9243,
780 <https://doi.org/10.5194/acp-22-9215-2022>, 2022.

781 Chen, H., Karion, A., Rella, C. W., Winderlich, J., Gerbig, C., Filges, A., Newberger, T.,
782 Sweeney, C., and Tans, P. P.: Accurate measurements of carbon monoxide in humid air using
783 the cavity ring-down spectroscopy (CRDS) technique, *Atmospheric Measurement*
784 *Techniques*, 6, 1031–1040, <https://doi.org/10.5194/amt-6-1031-2013>, 2013.

785 Chen, Y., Hall, J., Van Wees, D., Andela, N., Hantson, S., Giglio, L., Van Der Werf, G. R.,
786 Morton, D. C., and Randerson, J. T.: Multi-decadal trends and variability in burned area from
787 the fifth version of the Global Fire Emissions Database (GFED5), *Earth Syst. Sci. Data*, 15,
788 5227–5259, <https://doi.org/10.5194/essd-15-5227-2023>, 2023.

789 Crisp, D., Pollock, H. R., Rosenberg, R., Chapsky, L., Lee, R. A. M., Oyafuso, F. A.,
790 Frankenberg, C., O’Dell, C. W., Bruegge, C. J., Doran, G. B., Eldering, A., Fisher, B. M., Fu,
791 D., Gunson, M. R., Mandrake, L., Osterman, G. B., Schwandner, F. M., Sun, K., Taylor, T.
792 E., Wennberg, P. O., and Wunch, D.: The on-orbit performance of the Orbiting Carbon
793 Observatory-2 (OCO-2) instrument and its radiometrically calibrated products, *Atmos. Meas.*
794 *Tech.*, 10, 59–81, <https://doi.org/10.5194/amt-10-59-2017>, 2017.

795 Das, C., Kunchala, R. K., Chandra, N., Chhabra, A., and Pandya, M. R.: Characterizing the
796 regional XCO₂ variability and its association with ENSO over India inferred from GOSAT
797 and OCO-2 satellite observations, *Science of The Total Environment*, 902, 166176,
798 <https://doi.org/10.1016/j.scitotenv.2023.166176>, 2023.

799 Eldering, A., O’Dell, C. W., Wennberg, P. O., Crisp, D., Gunson, M. R., Viatte, C., Avis, C.,
800 Braverman, A., Castano, R., Chang, A., Chapsky, L., Cheng, C., Connor, B., Dang, L.,
801 Doran, G., Fisher, B., Frankenberg, C., Fu, D., Granat, R., Hobbs, J., Lee, R. A. M.,
802 Mandrake, L., McDuffie, J., Miller, C. E., Myers, V., Natraj, V., O’Brien, D., Osterman, G.

- 803 B., Oyafuso, F., Payne, V. H., Pollock, H. R., Polonsky, I., Roehl, C. M., Rosenberg, R.,
804 Schwandner, F., Smyth, M., Tang, V., Taylor, T. E., To, C., Wunch, D., and Yoshimizu, J.:
805 The Orbiting Carbon Observatory-2: first 18 months of science data products, *Atmos. Meas.*
806 *Tech.*, 10, 549–563, <https://doi.org/10.5194/amt-10-549-2017>, 2017.
- 807 Eldering, A., Taylor, T. E., O’Dell, C. W., and Pavlick, R.: The OCO-3 mission:
808 measurement objectives and expected performance based on 1 year of simulated data, *Atmos.*
809 *Meas. Tech.*, 12, 2341–2370, <https://doi.org/10.5194/amt-12-2341-2019>, 2019.
- 810 Fan, N., & Forkel, M. (2025). Drivers of the enhanced amplitude of atmospheric CO₂ in
811 northern terrestrial ecosystems. <https://doi.org/10.5194/egusphere-egu25-7279>
- 812 Fang, S. X., Tans, P. P., Steinbacher, M., Zhou, L. X., and Luan, T.: Comparison of the
813 regional CO₂ mole fraction filtering approaches at a WMO/GAW regional station in China,
814 *Atmospheric Measurement Techniques*, 8, 5301–5313, [https://doi.org/10.5194/amt-8-5301-](https://doi.org/10.5194/amt-8-5301-2015)
815 2015, 2015.
- 816 Fawzy, S., Osman, A. I., Doran, J., and Rooney, D. W.: Strategies for mitigation of climate
817 change: a review, *Environ Chem Lett*, 18, 2069–2094, [https://doi.org/10.1007/s10311-020-](https://doi.org/10.1007/s10311-020-01059-w)
818 01059-w, 2020.
- 819 Frankenberg, C., O’Dell, C., Berry, J., Guanter, L., Joiner, J., Köhler, P., Pollock, R., and
820 Taylor, T. E.: Prospects for chlorophyll fluorescence remote sensing from the Orbiting
821 Carbon Observatory-2, *Remote Sensing of Environment*, 147, 1–12,
822 <https://doi.org/10.1016/j.rse.2014.02.007>, 2014.
- 823 Friedlingstein, P., O’Sullivan, M., Jones, M. W., Andrew, R. M., Hauck, J., Landschützer, P.,
824 Le Quéré, C., Li, H., Luijkx, I. T., Olsen, A., Peters, G. P., Peters, W., Pongratz, J.,
825 Schwingshackl, C., Sitch, S., Canadell, J. G., Ciais, P., Jackson, R. B., Alin, S. R., Arneth, A.,
826 Arora, V., Bates, N. R., Becker, M., Bellouin, N., Berghoff, C. F., Bittig, H. C., Bopp, L.,
827 Cadule, P., Campbell, K., Chamberlain, M. A., Chandra, N., Chevallier, F., Chini, L. P.,
828 Colligan, T., Decayeux, J., Djeutchouang, L. M., Dou, X., Duran Rojas, C., Enyo, K., Evans,
829 W., Fay, A. R., Feely, R. A., Ford, D. J., Foster, A., Gasser, T., Gehlen, M., Gkritzalis, T.,
830 Grassi, G., Gregor, L., Gruber, N., Gürses, Ö., Harris, I., Hefner, M., Heinke, J., Hurtt, G. C.,
831 Iida, Y., Ilyina, T., Jacobson, A. R., Jain, A. K., Jarníková, T., Jersild, A., Jiang, F., Jin, Z.,
832 Kato, E., Keeling, R. F., Klein Goldewijk, K., Knauer, J., Korsbakken, J. I., Lan, X., Lauvset,
833 S. K., Lefèvre, N., Liu, Z., Liu, J., Ma, L., Maksyutov, S., Marland, G., Mayot, N., McGuire,
834 P. C., Metzl, N., Monacci, N. M., Morgan, E. J., Nakaoka, S.-I., Neill, C., Niwa, Y., Nützel,
835 T., Olivier, L., Ono, T., Palmer, P. I., Pierrot, D., Qin, Z., Resplandy, L., Roobaert, A.,
836 Rosan, T. M., Rödenbeck, C., Schwinger, J., Smallman, T. L., Smith, S. M., Sospedra-
837 Alfonso, R., Steinhoff, T., et al.: Global Carbon Budget 2024, *Earth Syst. Sci. Data*, 17, 965–
838 1039, <https://doi.org/10.5194/essd-17-965-2025>, 2025.
- 839 Halder, S., Tiwari, Y. K., Valsala, V., Sreeush, M. G., Sijikumar, S., Janardanan, R., &
840 Maksyutov, S. (2021). Quantification of enhancement in atmospheric CO₂ background due to
841 Indian biospheric fluxes and fossil fuel emissions. *Journal of Geophysical Research:*
842 *Atmospheres*, 126(13), e2021JD034545.
- 843 Harriss, R. C., Sachse, G. W., Collins Jr., J. E., Wade, L., Bartlett, K. B., Talbot, R. W.,
844 Browell, E. V., Barrie, L. A., Hill, G. F., and Burney, L. G.: Carbon monoxide and methane

- 845 over Canada: July–August 1990, *Journal of Geophysical Research: Atmospheres*, 99, 1659–
846 1669, <https://doi.org/10.1029/93JD01906>, 1994.
- 847 Huang, J., Golombek, A., Prinn, R., Weiss, R., Fraser, P., Simmonds, P., Dlugokencky, E. J.,
848 Hall, B., Elkins, J., Steele, P., Langenfelds, R., Krummel, P., Dutton, G., and Porter, L.:
849 Estimation of regional emissions of nitrous oxide from 1997 to 2005 using multinetwork
850 measurements, a chemical transport model, and an inverse method, *Journal of Geophysical*
851 *Research: Atmospheres*, 113, <https://doi.org/10.1029/2007JD009381>, 2008.
- 852 Huang, J., Yu, H., Guan, X., Wang, G., and Guo, R.: Accelerated dryland expansion under
853 climate change, *Nature Clim Change*, 6, 166–171, <https://doi.org/10.1038/nclimate2837>,
854 2016.
- 855 IPCC, 2021: *Climate Change 2021: The Physical Science Basis. Contribution of Working*
856 *Group I to the Sixth Assessment Report of the Intergovernmental Panel on Climate*
857 *Change*[Masson-Delmotte, V., P. Zhai, A. Pirani, S.L. Connors, C. Péan, S. Berger, N. Caud,
858 Y. Chen, L. Goldfarb, M.I. Gomis, M. Huang, K. Leitzell, E. Lonnoy, J.B.R. Matthews, T.K.
859 Maycock, T. Waterfield, O. Yelekçi, R. Yu, and B. Zhou (eds.)]. Cambridge University
860 Press, Cambridge, United Kingdom and New York, NY, USA, In press,
861 [doi:10.1017/9781009157896](https://doi.org/10.1017/9781009157896).
- 862 Ito, A.: Disequilibrium of terrestrial ecosystem CO₂ budget caused by disturbance-induced
863 emissions and non-CO₂ carbon export flows: a global model assessment, *Earth Syst. Dynam.*,
864 10, 685–709, <https://doi.org/10.5194/esd-10-685-2019>, 2019.
- 865 Jain, C. D., Singh, V., Akhil Raj, S. T., Madhavan, B. L., and Ratnam, M. V.: Local emission
866 and long-range transport impacts on the CO, CO₂, and CH₄ concentrations at a tropical rural
867 site, *Atmospheric Environment*, 254, 118397,
868 <https://doi.org/10.1016/j.atmosenv.2021.118397>, 2021.
- 869 Jing, X., Huang, J., Wang, G., Higuchi, K., Bi, J., Sun, Y., Yu, H., and Wang, T.: The effects
870 of clouds and aerosols on net ecosystem CO₂ exchange over semi-arid Loess Plateau of
871 Northwest China, *Atmospheric Chemistry and Physics*, 10, 8205–8218,
872 <https://doi.org/10.5194/acp-10-8205-2010>, 2010.
- 873 Joiner, J. and Yoshida, Y.: Satellite-based reflectances capture large fraction of variability in
874 global gross primary production (GPP) at weekly time scales, *Agricultural and Forest*
875 *Meteorology*, 291, 108092, <https://doi.org/10.1016/j.agrformet.2020.108092>, 2020.
- 876 Joiner, J., Yoshida, Y., Zhang, Y., Duveiller, G., Jung, M., Lyapustin, A., Wang, Y., and
877 Tucker, C. J.: Estimation of Terrestrial Global Gross Primary Production (GPP) with Satellite
878 Data-Driven Models and Eddy Covariance Flux Data, *Remote Sensing*, 10, 1346,
879 <https://doi.org/10.3390/rs10091346>, 2018.
- 880 Jones, M. W., Andrew, R. M., Peters, G. P., Janssens-Maenhout, G., De-Gol, A. J., Ciais, P.,
881 Patra, P. K., Chevallier, F., and Le Quéré, C.: Gridded fossil CO₂ emissions and related O₂
882 combustion consistent with national inventories 1959–2018, *Sci Data*, 8, 2,
883 <https://doi.org/10.1038/s41597-020-00779-6>, 2021.
- 884 Kar, J., Bremer, H., Drummond, J. R., Rochon, Y. J., Jones, D. B. A., Nichitiu, F., Zou, J.,
885 Liu, J., Gille, J. C., Edwards, D. P., Deeter, M. N., Francis, G., Ziskin, D., and Warner, J.:

886 Evidence of vertical transport of carbon monoxide from Measurements of Pollution in the
887 Troposphere (MOPITT), *Geophysical Research Letters*, 31,
888 <https://doi.org/10.1029/2004GL021128>, 2004.

889 Krishnapriya, M., Pattanaik, D. R., Kumar, A., Ramana, M. V., & Naidu, C. V. (2025).
890 Spatio-temporal dynamics of atmospheric CO₂ over India and its inter-relationship with
891 combustion emissions, ecosystem exchange, and meteorological factors: M Krishnapriya et
892 al. *Journal of Earth System Science*, 134(4), 193.

893 Krol, M., Houweling, S., Bregman, B., van den Broek, M., Segers, A., van Velthoven, P.,
894 Peters, W., Dentener, F., and Bergamaschi, P.: The two-way nested global chemistry-
895 transport zoom model TM5: algorithm and applications, *Atmospheric Chemistry and Physics*
896 *Discussions*, 4, 3975–4018, 2004.

897 Kumar, A., Yu, Z.-G., Klemeš, J. J., and Bokhari, A.: A state-of-the-art review of greenhouse
898 gas emissions from Indian hydropower reservoirs, *Journal of Cleaner Production*, 320,
899 128806, <https://doi.org/10.1016/j.jclepro.2021.128806>, 2021.

900 Kunchala, R. K., Girach, I., Das, C., Jain, C., Burman, P. K. D., Pathakoti, M., ... & Jain, V.
901 (2025). Carbon dioxide (CO₂) variations across India: Synthesis of observations and model
902 simulations. *Atmospheric Environment*, 121746.

903 Kunchala, R. K., Patra, P. K., Kumar, K. N., Chandra, N., Attada, R., and Karumuri, R. K.:
904 Spatio-temporal variability of XCO₂ over Indian region inferred from Orbiting Carbon
905 Observatory (OCO-2) satellite and Chemistry Transport Model, *Atmospheric Research*, 269,
906 106044, <https://doi.org/10.1016/j.atmosres.2022.106044>, 2022.

907 Kuttippurath, J., Peter, R., Singh, A., and Raj, S.: The increasing atmospheric CO₂ over
908 India: Comparison to global trends, *iScience*, 25, 104863,
909 <https://doi.org/10.1016/j.isci.2022.104863>, 2022.

910 Lai, S. C., Baker, A. K., Schuck, T. J., van Velthoven, P., Oram, D. E., Zahn, A., Hermann,
911 M., Weigelt, A., Slemr, F., Brenninkmeijer, C. a. M., and Ziereis, H.: Pollution events
912 observed during CARIBIC flights in the upper troposphere between South China and the
913 Philippines, *Atmospheric Chemistry and Physics*, 10, 1649–1660,
914 <https://doi.org/10.5194/acp-10-1649-2010>, 2010.

915 Le Quéré, C., Andrew, R. M., Friedlingstein, P., Sitch, S., Pongratz, J., Manning, A. C.,
916 Korsbakken, J. I., Peters, G. P., Canadell, J. G., Jackson, R. B., Boden, T. A., Tans, P. P.,
917 Andrews, O. D., Arora, V. K., Bakker, D. C. E., Barbero, L., Becker, M., Betts, R. A., Bopp,
918 L., Chevallier, F., Chini, L. P., Ciais, P., Cosca, C. E., Cross, J., Currie, K., Gasser, T., Harris,
919 I., Hauck, J., Haverd, V., Houghton, R. A., Hunt, C. W., Hurtt, G., Ilyina, T., Jain, A. K.,
920 Kato, E., Kautz, M., Keeling, R. F., Klein Goldewijk, K., Körtzinger, A., Landschützer, P.,
921 Lefèvre, N., Lenton, A., Lienert, S., Lima, I., Lombardozzi, D., Metzl, N., Millero, F.,
922 Monteiro, P. M. S., Munro, D. R., Nabel, J. E. M. S., Nakaoka, S., Nojiri, Y., Padin, X. A.,
923 Peregón, A., Pfeil, B., Pierrot, D., Poulter, B., Rehder, G., Reimer, J., Rödenbeck, C.,
924 Schwinger, J., Séférian, R., Skjelvan, I., Stocker, B. D., Tian, H., Tilbrook, B., Tubiello, F.
925 N., Van Der Laan-Luijkx, I. T., Van Der Werf, G. R., Van Heuven, S., Viovy, N., Vuichard,
926 N., Walker, A. P., Watson, A. J., Wiltshire, A. J., Zaehle, S., and Zhu, D.: Global Carbon
927 Budget 2017, *Earth Syst. Sci. Data*, 10, 405–448, <https://doi.org/10.5194/essd-10-405-2018>,
928 2018.

- 929 ICOS RI, 2020. ICOS Atmosphere Station Specifications V2.0 (editor: O. Laurent). ICOS
930 ERIC. <https://doi.org/10.18160/GK28-2188>
931
- 932 Lin, X., Indira, N. K., Ramonet, M., Delmotte, M., Ciais, P., Bhatt, B. C., Reddy, M. V.,
933 Anghuk, D., Balakrishnan, S., Jorphail, S., Dorjai, T., Mahey, T. T., Patnaik, S., Begum, M.,
934 Brenninkmeijer, C., Durairaj, S., Kirubakaran, R., Schmidt, M., Swathi, P. S., Vinithkumar,
935 N. V., Yver Kwok, C., and Gaur, V. K.: Long-lived atmospheric trace gases measurements in
936 flask samples from three stations in India, *Atmos. Chem. Phys.*, 15, 9819–9849,
937 <https://doi.org/10.5194/acp-15-9819-2015>, 2015.
- 938 Lin, X., Ciais, P., Bousquet, P., Ramonet, M., Yin, Y., Balkanski, Y., Cozic, A., Delmotte,
939 M., Evangelou, N., Indira, N. K., Locatelli, R., Peng, S., Piao, S., Saunio, M., Swathi, P. S.,
940 Wang, R., Yver-Kwok, C., Tiwari, Y. K., and Zhou, L.: Simulating CH₄ and CO₂ over South
941 and East Asia using the zoomed chemistry transport model LMDz-INCA, *Atmos. Chem.*
942 *Phys.*, 18, 9475–9497, <https://doi.org/10.5194/acp-18-9475-2018>, 2018.
- 943 Liu, J., Bowman, K. W., Lee, M., Henze, D. K., Bousserez, N., Brix, H., Collatz, G. J.,
944 Menemenlis, D., Ott, L., Pawson, S., Jones, D., and Nassar, R.: Carbon monitoring system
945 flux estimation and attribution: impact of ACOS-GOSAT XCO₂ sampling on the inference of
946 terrestrial biospheric sources and sinks, *Tellus B: Chemical and Physical Meteorology*, 66,
947 22486, <https://doi.org/10.3402/tellusb.v66.22486>, 2014.
- 948 Lopez, M.: Estimation des émissions de gaz à effet de serre à différentes échelles en France à
949 l'aide d'observations de haute précision, phdthesis, Université Paris Sud - Paris XI, 2012.
- 950 Mahesh, P., Sreenivas, G., Rao, P. V. N., Dadhwal, V. K., Sai Krishna, S. V. S., and
951 Mallikarjun, K.: High-precision surface-level CO₂ and CH₄ using off-axis integrated cavity
952 output spectroscopy (OA-ICOS) over Shadnagar, India, *International Journal of Remote*
953 *Sensing*, 36, 5754–5765, <https://doi.org/10.1080/01431161.2015.1104744>, 2015.
- 954 Mangaraj, P., Matsumi, Y., Nakayama, T., Biswal, A., Yamaji, K., Araki, H., ... & Mor, S.
955 (2025). Weak coupling of observed surface PM_{2.5} in Delhi-NCR with rice crop residue
956 burning in Punjab and Haryana. *Npj Climate and Atmospheric Science*, 8(1), 18.
- 957 Masarie, K. A., Peters, W., Jacobson, A. R., and Tans, P. P.: ObsPack: a framework for the
958 preparation, delivery, and attribution of atmospheric greenhouse gas measurements, *Earth*
959 *Syst. Sci. Data*, 6, 375–384, <https://doi.org/10.5194/essd-6-375-2014>, 2014.
- 960 Matsueda, H., Inoue, H. Y., Ishii, M., and Tsutsumi, Y.: Large injection of carbon monoxide
961 into the upper troposphere due to intense biomass burning in 1997, *J. Geophys. Res.*, 104,
962 26867–26879, <https://doi.org/10.1029/1999JD900193>, 1999.
- 963 Mauzerall, D. L., Logan, J. A., Jacob, D. J., Anderson, B. E., Blake, D. R., Bradshaw, J. D.,
964 Heikes, B., Sachse, G. W., Singh, H., and Talbot, B.: Photochemistry in biomass burning
965 plumes and implications for tropospheric ozone over the tropical South Atlantic, *J. Geophys.*
966 *Res.*, 103, 8401–8423, <https://doi.org/10.1029/97JD02612>, 1998.
- 967 Metya, A., Datye, A., Chakraborty, S., Tiwari, Y. K., Sarma, D., Bora, A., and Gogoi, N.:
968 Diurnal and seasonal variability of CO₂ and CH₄ concentration in a semi-urban environment
969 of western India, *Sci Rep*, 11, 2931, <https://doi.org/10.1038/s41598-021-82321-1>, 2021.

- 970 Mühle, J., Brenninkmeijer, C. a. M., Rhee, T. S., Slemr, F., Oram, D. E., Penkett, S. A., and
971 Zahn, A.: Biomass burning and fossil fuel signatures in the upper troposphere observed
972 during a CARIBIC flight from Namibia to Germany, *Geophysical Research Letters*, 29, 16-1-
973 16-4, <https://doi.org/10.1029/2002GL015764>, 2002.
- 974 Munksgaard, N. C., Lee, I. L., Napier, T. P., Zwart, C., Cernusak, L. A., & Bird, M. I. (2022).
975 One year of spectroscopic high-frequency measurements of atmospheric CO₂, CH₄, H.
976 *Geoscience Data Journal*. <https://doi.org/10.1002/gdj3.180>
- 977 Nalini, K., Sijikumar, S., Valsala, V., Tiwari, Y. K., and Ramachandran, R.: Designing
978 surface CO₂ monitoring network to constrain the Indian land fluxes, *Atmospheric*
979 *Environment*, 218, 117003, <https://doi.org/10.1016/j.atmosenv.2019.117003>, 2019.
- 980 Nath, B.: Quantitative Assessment of Forest Cover Change of a Part of Bandarban Hill Tracts
981 Using NDVI Techniques, *Journal of Geosciences and Geomatics*, 2, 21–27,
982 <https://doi.org/10.12691/jgg-2-1-4>, 2014.
- 983 Nishanth, T., Praseed, K. M., Kumar, M. K. S., and Valsaraj, K. T.: Observational Study of
984 Surface O₃, NO_x, CH₄ and Total NMHCs at Kannur, India, *Aerosol Air Qual. Res.*, 14,
985 1074–1088, <https://doi.org/10.4209/aaqr.2012.11.0323>, 2014.
- 986 Niwa, Y., Machida, T., Sawa, Y., Matsueda, H., Schuck, T. J., Brenninkmeijer, C. A. M.,
987 Imasu, R., and Satoh, M.: Imposing strong constraints on tropical terrestrial CO₂ fluxes using
988 passenger aircraft based measurements, *Journal of Geophysical Research: Atmospheres*, 117,
989 <https://doi.org/10.1029/2012JD017474>, 2012.
- 990 Nomura, S., Naja, M., Ahmed, M. K., Mukai, H., Terao, Y., Machida, T., Sasakawa, M., and
991 Patra, P. K.: Measurement report: Regional characteristics of seasonal and long-term
992 variations in greenhouse gases at Nainital, India, and Comilla, Bangladesh, *Atmos. Chem.*
993 *Phys.*, 21, 16427–16452, <https://doi.org/10.5194/acp-21-16427-2021>, 2021.
- 994 Paris, J.-D., Ciais, P., Nédélec, P., Ramonet, M., Belan, B. D., Arshinov, M. Yu., Golitsyn, G.
995 S., Granberg, I., Stohl, A., Cayez, G., Athier, G., Boumard, F., and Cousin, J.-M.: The YAK-
996 AEROSIB transcontinental aircraft campaigns: new insights on the transport of CO₂, CO and
997 O₃ across Siberia, *Tellus B: Chemical and Physical Meteorology*, 60, 551–568,
998 <https://doi.org/10.1111/j.1600-0889.2008.00369.x>, 2008.
- 999 Park, M., Randel, W. J., Emmons, L. K., and Livesey, N. J.: Transport pathways of carbon
1000 monoxide in the Asian summer monsoon diagnosed from Model of Ozone and Related
1001 Tracers (MOZART), *J. Geophys. Res.*, 114, 2008JD010621,
1002 <https://doi.org/10.1029/2008JD010621>, 2009.
- 1003 Pathakoti, M., D.V., M., Gaddamidi, S., Arun, S. S., Bothale, R. V., Chauhan, P., P, R., K.S.,
1004 R., and Chandra, N.: Three-dimensional view of CO₂ variability in the atmosphere over the
1005 Indian region, *Atmospheric Research*, 290, 106785,
1006 <https://doi.org/10.1016/j.atmosres.2023.106785>, 2023.
- 1007 Patil, M. N., Dharmaraj, T., Waghmare, R. T., Prabha, T. V., and Kulkarni, J. R.:
1008 Measurements of carbon dioxide and heat fluxes during monsoon-2011 season over rural site
1009 of India by eddy covariance technique, *J Earth Syst Sci*, 123, 177–185,
1010 <https://doi.org/10.1007/s12040-013-0374-z>, 2014.

- 1011 Patra, P. K., Niwa, Y., Schuck, T. J., Brenninkmeijer, C. a. M., Machida, T., Matsueda, H.,
1012 and Sawa, Y.: Carbon balance of South Asia constrained by passenger aircraft CO₂
1013 measurements, *Atmospheric Chemistry and Physics*, 11, 4163–4175,
1014 <https://doi.org/10.5194/acp-11-4163-2011>, 2011.
- 1015 Patra, P. K., Canadell, J. G., Houghton, R. A., Piao, S. L., Oh, N.-H., Ciais, P., Manjunath, K.
1016 R., Chhabra, A., Wang, T., Bhattacharya, T., Bousquet, P., Hartman, J., Ito, A., Mayorga, E.,
1017 Niwa, Y., Raymond, P. A., Sarma, V. V. S. S., and Lasco, R.: The carbon budget of South
1018 Asia, *Biogeosciences*, 10, 513–527, <https://doi.org/10.5194/bg-10-513-2013>, 2013.
- 1019 Patra, P. K., Crisp, D., Kaiser, J. W., Wunch, D., Saeki, T., Ichii, K., Sekiya, T., Wennberg,
1020 P. O., Feist, D. G., Pollard, D. F., Griffith, D. W. T., Velasco, V. A., De Maziere, M., Sha, M.
1021 K., Roehl, C., Chatterjee, A., and Ishijima, K.: The Orbiting Carbon Observatory (OCO-2)
1022 tracks 2–3 peta-gram increase in carbon release to the atmosphere during the 2014–2016 El
1023 Niño, *Sci Rep*, 7, 13567, <https://doi.org/10.1038/s41598-017-13459-0>, 2017.
- 1024 Patra, P. K., Takigawa, M., Watanabe, S., Chandra, N., Ishijima, K., and Yamashita, Y.:
1025 Improved Chemical Tracer Simulation by MIROC4.0-based Atmospheric Chemistry-
1026 Transport Model (MIROC4-ACTM), *Sola*, 14, 91–96, <https://doi.org/10.2151/sola.2018-016>,
1027 2018.
- 1028 Peters, W., Miller, J. B., Whitaker, J., Denning, A. S., Hirsch, A., Krol, M. C., Zupanski, D.,
1029 Bruhwiler, L., and Tans, P. P.: An ensemble data assimilation system to estimate CO₂ surface
1030 fluxes from atmospheric trace gas observations, *Journal of Geophysical Research:*
1031 *Atmospheres*, 110, <https://doi.org/10.1029/2005JD006157>, 2005.
- 1032 Philip, S., Johnson, M. S., Potter, C., Genovesse, V., Baker, D. F., Haynes, K. D., Henze, D.
1033 K., Liu, J., and Poulter, B.: Prior biosphere model impact on global terrestrial CO₂ fluxes
1034 estimated from OCO-2 retrievals, *Atmos. Chem. Phys.*, 19, 13267–13287,
1035 <https://doi.org/10.5194/acp-19-13267-2019>, 2019.
- 1036 Philip, S., Johnson, M. S., Baker, D. F., Basu, S., Tiwari, Y. K., Indira, N. K., Ramonet, M.,
1037 and Poulter, B.: OCO-2 Satellite-Imposed Constraints on Terrestrial Biospheric CO₂ Fluxes
1038 Over South Asia, *JGR Atmospheres*, 127, e2021JD035035,
1039 <https://doi.org/10.1029/2021JD035035>, 2022.
- 1040 Potter, C. S., Randerson, J. T., Field, C. B., Matson, P. A., Vitousek, P. M., Mooney, H. A.,
1041 and Klooster, S. A.: Terrestrial ecosystem production: A process model based on global
1042 satellite and surface data, *Global Biogeochemical Cycles*, 7, 811–841,
1043 <https://doi.org/10.1029/93GB02725>, 1993.
- 1044 Randel, W. J. and Park, M.: Deep convective influence on the Asian summer monsoon
1045 anticyclone and associated tracer variability observed with Atmospheric Infrared Sounder
1046 (AIRS), *Journal of Geophysical Research: Atmospheres*, 111,
1047 <https://doi.org/10.1029/2005JD006490>, 2006.
- 1048 Randerson, J. T., Thompson, M. V., Conway, T. J., Fung, I. Y., and Field, C. B.: The
1049 contribution of terrestrial sources and sinks to trends in the seasonal cycle of atmospheric
1050 carbon dioxide, *Global Biogeochemical Cycles*, 11, 535–560,
1051 <https://doi.org/10.1029/97GB02268>, 1997.

- 1052 Rathore, J., Ganguly, D., Singh, V., Gupta, M., Vazhathara, V. J., Biswal, A., Kunchala, R.
1053 K., Patra, P. K., Sahu, L. K., Gani, S., and Dey, S.: Characteristics of Haze Pollution Events
1054 During Biomass Burning Period at an Upwind Site of Delhi, *JGR Atmospheres*, 130,
1055 e2024JD042347, <https://doi.org/10.1029/2024JD042347>, 2025.
- 1056 Rayner, P. J., Law, R. M., Allison, C. E., Francey, R. J., Trudinger, C. M., and Pickett-Heaps,
1057 C.: Interannual variability of the global carbon cycle (1992–2005) inferred by inversion of
1058 atmospheric CO₂ and $\delta^{13}\text{C}_{\text{CO}_2}$ measurements, *Global Biogeochemical Cycles*, 22,
1059 <https://doi.org/10.1029/2007GB003068>, 2008.
- 1060 Reid, K. H. and Steyn, D. G.: Diurnal variations of boundary-layer carbon dioxide in a
1061 coastal city—Observations and comparison with model results, *Atmospheric Environment*,
1062 31, 3101–3114, [https://doi.org/10.1016/S1352-2310\(97\)00050-2](https://doi.org/10.1016/S1352-2310(97)00050-2), 1997.
- 1063 Russo, R. S., Talbot, R. W., Dibb, J. E., Scheuer, E., Seid, G., Jordan, C. E., Fuelberg, H. E.,
1064 Sachse, G. W., Avery, M. A., Vay, S. A., Blake, D. R., Blake, N. J., Atlas, E., Fried, A.,
1065 Sandholm, S. T., Tan, D., Singh, H. B., Snow, J., and Heikes, B. G.: Chemical composition
1066 of Asian continental outflow over the western Pacific: Results from Transport and Chemical
1067 Evolution over the Pacific (TRACE-P), *Journal of Geophysical Research: Atmospheres*, 108,
1068 <https://doi.org/10.1029/2002JD003184>, 2003.
- 1069 Sawa, Y., Matsueda, H., Makino, Y., Inoue, H. Y., Murayama, S., Hirota, M., Tsutsumi, Y.,
1070 Zaizen, Y., Ikegami, M., and Okada, K.: Aircraft Observation of CO₂, CO₂ O₃ and H₂ over
1071 the North Pacific during the PACE-7 Campaign, *Tellus B: Chemical and Physical*
1072 *Meteorology*, 56, 2, <https://doi.org/10.3402/tellusb.v56i1.16402>, 2004.
- 1073 Schaaf, C. and Wang, Z.: MODIS/Terra+Aqua BRDF/Albedo Nadir BRDF-Adjusted Ref
1074 Band6 Daily L3 Global 30ArcSec CMG V061,
1075 <https://doi.org/10.5067/MODIS/MCD43D67.061>, 2021.
- 1076 Schaaf, C. B., Gao, F., Strahler, A. H., Lucht, W., Li, X., Tsang, T., Strugnell, N. C., Zhang,
1077 X., Jin, Y., Muller, J.-P., Lewis, P., Barnsley, M., Hobson, P., Disney, M., Roberts, G.,
1078 Dunderdale, M., Doll, C., d’Entremont, R. P., Hu, B., Liang, S., Privette, J. L., and Roy, D.:
1079 First operational BRDF, albedo nadir reflectance products from MODIS, *Remote Sensing of*
1080 *Environment*, 83, 135–148, [https://doi.org/10.1016/S0034-4257\(02\)00091-3](https://doi.org/10.1016/S0034-4257(02)00091-3), 2002.
- 1081 Schuck, T. J., Ishijima, K., Patra, P. K., Baker, A. K., Machida, T., Matsueda, H., Sawa, Y.,
1082 Umezawa, T., Brenninkmeijer, C. a. M., and Lelieveld, J.: Distribution of methane in the
1083 tropical upper troposphere measured by CARIBIC and CONTRAIL aircraft, *Journal of*
1084 *Geophysical Research: Atmospheres*, 117, <https://doi.org/10.1029/2012JD018199>, 2012.
- 1085 Schuldt, K. N., Mund, J., Aalto, T., Abshire, J. B., Aikin, K., Allen, G., Andrade, M., Arlyn
1086 Andrews, Apadula, F., Arnold, S., Baier, B., Bakwin, P., Bani, L., Bartyzel, J., Bentz, G.,
1087 Bergamaschi, P., Beyersdorf, A., Biermann, T., Biraud, S. C., Pierre-Eric Blanc, Boenisch,
1088 H., Bowling, D., Brailsford, G., Brand, W. A., Brunner, D., Bui, T. P. V., Van Den Bulk, P.,
1089 Benoit Burban, Francescopiero Calzolari, Chang, C. S., Chen, G., Huilin Chen, Lukasz
1090 Chmura, St. Clair, J. M., Clark, S., Sites Climadat, Coletta, J. D., Colomb, A., Commane, R.,
1091 Condori, L., Conen, F., Conil, S., Couret, C., Cristofanelli, P., Cuevas, E., Curcoll, R., Daube,
1092 B., Davis, K. J., Dean-Day, J. M., Delmotte, M., Dickerson, R., DiGangi, E., DiGangi, J. P.,
1093 Van Dinter, D., Elsasser, M., Emmenegger, L., Shuangxi Fang, Forster, G., France, J.,
1094 Frumau, A., Fuente-Lastra, M., Galkowski, M., Gatti, L. V., Gehrlein, T., Gerbig, C.,

- 1095 Francois Gheusi, Gloor, E., Goto, D., Griffis, T., Hammer, S., Hanisco, T. F., Hanson, C.,
 1096 Haszpra, L., Hatakka, J., Heimann, M., Heliasz, M., Heltai, D., Henne, S., Hensen, A.,
 1097 Hermans, C., Hermansen, O., Hintsa, E., Hoheisel, A., Holst, J., Di Iorio, T., Iraci, L. T.,
 1098 Ivakhov, V., Jaffe, D. A., Jordan, A., Joubert, W., Kang, H.-Y., Karion, A., Kawa, S. R.,
 1099 Kazan, V., Keeling, R. F., Keronen, P., Jooil Kim, Klausen, J., Kneuer, T., et al.: Multi-
 1100 laboratory compilation of atmospheric carbon dioxide data for the period 1957-2023;
 1101 obspack_co2_1_GLOBALVIEWplus_v10.1_2024-11-13,
 1102 <https://doi.org/10.25925/20241101>, 2024.
- 1103 Sharma, N., Dadhwal, V. K., Kant, Y., Mahesh, P., Mallikarjun, K., Gadavi, H., Sharma, A.,
 1104 and Ali, M. M.: Atmospheric CO₂ Variations in Two Contrasting Environmental Sites Over
 1105 India, *Air, Soil and Water Research*, 7, ASWR.S13987,
 1106 <https://doi.org/10.4137/ASWR.S13987>, 2014.
- 1107 Sreenivas, G., Mahesh, P., Subin, J., Kanchana, A. L., Rao, P. V. N., and Dadhwal, V. K.:
 1108 Influence of Meteorology and interrelationship with greenhouse gases
 1109 (CO₂ and CH₄) at a suburban site of India,
 1110 *Atmos. Chem. Phys.*, 16, 3953–3967, <https://doi.org/10.5194/acp-16-3953-2016>, 2016.
- 1111 Sreenivas, G., P., M., Mahalakshmi, D. V., Kanchana, A. L., Chandra, N., Patra, P. K., Raja,
 1112 P., Sesha Sai, M. V. R., Sripada, S., Rao, P. V. N., and Dadhwal, V. K.: Seasonal and annual
 1113 variations of CO₂ and CH₄ at Shadnagar, a semi-urban site, *Science of The Total*
 1114 *Environment*, 819, 153114, <https://doi.org/10.1016/j.scitotenv.2022.153114>, 2022.
- 1115 Srivastava, P., Bennett, M. W., Bedrosian, G., Rosenberg, R., Solish, B., and Basilio, R. R.:
 1116 Establishing Launch Readiness of NASA ISS Instrument OCO-3, in: *IGARSS 2020 - 2020*
 1117 *IEEE International Geoscience and Remote Sensing Symposium, IGARSS 2020 - 2020 IEEE*
 1118 *International Geoscience and Remote Sensing Symposium, Waikoloa, HI, USA*, 6101–6104,
 1119 <https://doi.org/10.1109/IGARSS39084.2020.9323631>, 2020.
- 1120 Stocker, T.F., D. Qin, G.-K. Plattner, L.V. Alexander, S.K. Allen, N.L. Bindoff, F.-M. Bréon,
 1121 J.A. Church, U. Cubasch, S. Emori, P. Forster, P. Friedlingstein, N. Gillett, J.M. Gregory,
 1122 D.L. Hartmann, E. Jansen, B. Kirtman, R. Knutti, K. Krishna Kumar, P. Lemke, J. Marotzke,
 1123 V. Masson-Delmotte, G.A. Meehl, I.I. Mokhov, S. Piao, V. Ramaswamy, D. Randall, M.
 1124 Rhein, M. Rojas, C. Sabine, D. Shindell, L.D. Talley, D.G. Vaughan and S.-P. Xie, 2013:
 1125 Technical Summary. In: *Climate Change 2013: The Physical Science Basis. Contribution of*
 1126 *Working Group I to the Fifth Assessment Report of the Intergovernmental Panel on Climate*
 1127 *Change* [Stocker, T.F., D. Qin, G.-K. Plattner, M. Tignor, S.K. Allen, J. Boschung, A.
 1128 Nauels, Y. Xia, V. Bex and P.M. Midgley (eds.)]. Cambridge University Press, Cambridge,
 1129 United Kingdom and New York, NY, USA
- 1130 Stull, R. B. (Ed.): *An Introduction to Boundary Layer Meteorology*, Springer Netherlands,
 1131 Dordrecht, <https://doi.org/10.1007/978-94-009-3027-8>, 1988.
- 1132 Summa, D., Di Girolamo, P., Stelitano, D., and Cacciani, M.: Characterization of the
 1133 planetary boundary layer height and structure by Raman lidar: comparison of different
 1134 approaches, *Atmospheric Measurement Techniques*, 6, 3515–3525,
 1135 <https://doi.org/10.5194/amt-6-3515-2013>, 2013.
- 1136 Sun, Y., Frankenberg, C., Jung, M., Joiner, J., Guanter, L., Köhler, P., and Magney, T.:
 1137 Overview of Solar-Induced chlorophyll Fluorescence (SIF) from the Orbiting Carbon

- 1138 Observatory-2: Retrieval, cross-mission comparison, and global monitoring for GPP, Remote
1139 Sensing of Environment, 209, 808–823, <https://doi.org/10.1016/j.rse.2018.02.016>, 2018.
- 1140 Thilakan, V., Pillai, D., Sukumaran, J., Gerbig, C., Hakkim, H., Sinha, V., Terao, Y., Naja,
1141 M., and Deshpande, M. V.: Potential of using CO₂ observations over India in regional carbon
1142 budget estimation by improving the modelling system, EGU sphere, 1–32,
1143 <https://doi.org/10.5194/egusphere-2023-1582>, 2023.
- 1144 Tiwari, Y., Valsala, V., Vellore, R., and Kunchala, R.: Effectiveness of surface monitoring
1145 stations in representing regional CO₂ emissions over India, Clim. Res., 56, 121–129,
1146 <https://doi.org/10.3354/cr01149>, 2013.
- 1147 Tiwari, Y. K., Vellore, R. K., Ravi Kumar, K., Van Der Schoot, M., and Cho, C.-H.:
1148 Influence of monsoons on atmospheric CO₂ spatial variability and ground-based monitoring
1149 over India, Science of The Total Environment, 490, 570–578,
1150 <https://doi.org/10.1016/j.scitotenv.2014.05.045>, 2014.
- 1151 Vermote, E. and NOAA CDR Program: NOAA Climate Data Record (CDR) of AVHRR
1152 Normalized Difference Vegetation Index (NDVI), Version 5,
1153 <https://doi.org/10.7289/V5ZG6QH9>, 2018.
- 1154 Wada, A., Matsueda, H., Sawa, Y., Tsuboi, K., and Okubo, S.: Seasonal variation of
1155 enhancement ratios of trace gases observed over 10 years in the western North Pacific,
1156 Atmospheric Environment, 45, 2129–2137, <https://doi.org/10.1016/j.atmosenv.2011.01.043>,
1157 2011.
- 1158 Wang, G., Huang, J., Guo, W., Zuo, J., Wang, J., Bi, J., Huang, Z., and Shi, J.: Observation
1159 analysis of land-atmosphere interactions over the Loess Plateau of northwest China, Journal
1160 of Geophysical Research: Atmospheres, 115, <https://doi.org/10.1029/2009JD013372>, 2010.
- 1161 Wang, Z., Schaaf, C. B., Sun, Q., Shuai, Y., and Román, M. O.: Capturing rapid land surface
1162 dynamics with Collection V006 MODIS BRDF/NBAR/Albedo (MCD43) products, Remote
1163 Sensing of Environment, 207, 50–64, <https://doi.org/10.1016/j.rse.2018.02.001>, 2018.
- 1164 Watanabe, S., Miura, H., Sekiguchi, M., Nagashima, T., Sudo, K., Emori, S., and Kawamiya,
1165 M.: Development of an atmospheric general circulation model for integrated Earth system
1166 modeling on the Earth Simulator, Earth Simulator, 9, 27–35, 2008.
- 1167 Wigley, T. M. L. (1983). The pre-industrial carbon dioxide level. *Climatic change*, 5(4), 315-
1168 320.
- 1169 Worthy, D. E. J., Chan, E., Ishizawa, M., Chan, D., Poss, C., Dlugokencky, E. J., Maksyutov,
1170 S., and Levin, I.: Decreasing anthropogenic methane emissions in Europe and Siberia inferred
1171 from continuous carbon dioxide and methane observations at Alert, Canada, Journal of
1172 Geophysical Research: Atmospheres, 114, <https://doi.org/10.1029/2008JD011239>, 2009.
- 1173 Xiao, Y., Jacob, D. J., Wang, J. S., Logan, J. A., Palmer, P. I., Suntharalingam, P., Yantosca,
1174 R. M., Sachse, G. W., Blake, D. R., and Streets, D. G.: Constraints on Asian and European
1175 sources of methane from CH₄-C₂H₆-CO correlations in Asian outflow, J. Geophys. Res.,
1176 109, 2003JD004475, <https://doi.org/10.1029/2003JD004475>, 2004.

- 1177 Xiong, X., Houweling, S., Wei, J., Maddy, E., Sun, F., and Barnet, C.: Methane plume over
1178 south Asia during the monsoon season: satellite observation and model simulation,
1179 *Atmospheric Chemistry and Physics*, 9, 783–794, <https://doi.org/10.5194/acp-9-783-2009>,
1180 2009.
- 1181 Yoro, K. O. and Daramola, M. O.: CO₂ emission sources, greenhouse gases, and the global
1182 warming effect, in: *Advances in Carbon Capture*, Elsevier, 3–28,
1183 <https://doi.org/10.1016/B978-0-12-819657-1.00001-3>, 2020.
- 1184 Yuan, Y., Ries, L., Petermeier, H., Steinbacher, M., Gómez-Peláez, A. J., Leuenberger, M.
1185 C., Schumacher, M., Trickl, T., Couret, C., Meinhardt, F., and Menzel, A.: Adaptive selection
1186 of diurnal minimum variation: a statistical strategy to obtain representative atmospheric CO₂
1187 data and its application to European elevated mountain stations, *Atmospheric Measurement*
1188 *Techniques*, 11, 1501–1514, <https://doi.org/10.5194/amt-11-1501-2018>, 2018.
- 1189 Zhang, H. F., Chen, B. Z., van der Laan-Luijk, I. T., Machida, T., Matsueda, H., Sawa, Y.,
1190 Fukuyama, Y., Langenfelds, R., van der Schoot, M., Xu, G., Yan, J. W., Cheng, M. L., Zhou,
1191 L. X., Tans, P. P., and Peters, W.: Estimating Asian terrestrial carbon fluxes from
1192 CONTRAIL aircraft and surface CO₂ observations for the period 2006–2010,
1193 *Atmospheric Chemistry and Physics*, 14, 5807–5824, [https://doi.org/10.5194/acp-14-5807-](https://doi.org/10.5194/acp-14-5807-2014)
1194 2014, 2014.
- 1195 Zhang, X., Nakazawa, T., Ishizawa, M., Aoki, S., Nakaoka, S.-I., Sugawara, S., Maksyutov,
1196 S., Saeki, T., and Hayasaka, T.: Temporal variations of atmospheric carbon dioxide in the
1197 southernmost part of Japan, *Tellus B: Chemical and Physical Meteorology*, 59, 654–663,
1198 <https://doi.org/10.1111/j.1600-0889.2007.00288.x>, 2007.
- 1199